Velocity field and parametric analysis of a subsonic, medium-Reynolds number cavity flow

Thierry M. Faure*

Université Pierre et Marie Curie, Sorbonne Universités,
4 place Jussieu, 75252 Paris Cedex 05, France
Université Paris-Sud,
91405 Orsay Cedex, France
Laboratoire d'Informatique pour la Mécanique et les Sciences de l'Ingénieur,
Unité Propre de Recherche 3251, Centre National de la Recherche Scientifique
bât. 508 rue J. Von Neumann, B.P. 133, 91403 Orsay Cedex, France
**current address: Centre de Recherche de l'Armée de l'air (CReA)*
École de l'Air, B.A. 701, 13661 Salon-de-Provence, France

Communicating author: Thierry M. Faure
e-mail: thierry.faure@limsi.fr
thierry-m.faure@inet.air.defense.gouv.fr
telephone: (33) 4 90 17 80 00 (+26 040)
fax: (33) 4 90 17 81 89

Abstract

Cavity flows are a class of flows bounded by material structures, where a recirculation region is present, and they are found in many practical applications. In the present study, the interaction between a boundary layer and an open parallelepipedic cavity develops a Kelvin-Helmholtz-like instability coupled with the cavity recirculation. PIV measurements of the flow are carried out in two orthogonal planes inside the cavity, for different aspect ratios, incompressible flow conditions and Reynolds numbers in the range 1900 to 12000. Mean velocity and second-order moments of velocity fluctuations reveal the flow morphology. For particular conditions, centrifugal instabilities appear that are induced by flow curvature due to wall confinement. The use of an identification criterion indicates the presence of pairs of counter-rotating vortices winded around the recirculation. A parametric analysis is conducted and the inviscid Rayleigh discriminant provides the potentially unstable flow regions inside the cavity. Finally, a stability parameter considering the ratio between centrifugal destabilizing effects and stabilizing viscous effects is carried out, and gives thresholds for the emergence of the centrifugal instability. The study draws to an end with a comparison with a well-documented lid-driven cavity flow.

1 Introduction

Cavity flows are a wide class of wall-bounded flows dominated by recirculation vortices which have received significant attention in the past years. They are found, with medium-range Reynolds numbers, in various applications:

- wind transport pollutant in streets surrounded with buildings (Chabni, 1997);
- cooling systems over integrated circuits made of parallelepipedic electronics components;
- door gaps on motor vehicles (Reulet et al., 2002);
- insects wings with small cavities or riblets on a wing, increasing lift without drag penalty (Buckholz, 1986);
- hydrodynamic bearings and lubricating systems (Braun et al., 1993);

– artificial aortic devices or blood aneurysms (Liou & Liao, 1997).

A completed synthesis on cavity flows and noise generation is given in Gloerfelt (2009). It is possible to distinguish between lid-driven cavity flows (Migeon, 2000, Guermond et al., 2002, Migeon, 2002, Migeon et al., 2003, Siegmann-Hegerfeld et al. 2013), and shear-layer cavity flows (Fang et al., 1999, Lin & Rockwell, 2001, Forestier et al. 2003, Larchevêque et al., 2004, Kegerise et al., 2004, Savelsberg & Castro, 2008, Haigermoser et al., 2009). Among these latter, it is possible to divide them, after Charwat et al. (1961), between open cavities, where the shear-layer interacts with the downstream edge of the cavity, and closed cavities, with flow reattachment on the cavity bottom. The boundary between these two classes is found for a cavity length-to-depth ratio varying from 8 (Sarohia, 1977) to 11 (Charwat et al., 1961). The open cavity issue develops a Kelvin-Helmholtz-like instability above a cavity flow featuring a primary spanwise recirculation vortex. The internal cavity flow itself is subject to develop a centrifugal instability and vortical features. We can build three Reynolds numbers with the external upstream flow velocity U_e and the fluid viscosity ν depending on the phenomenon considered. $Re_{\delta 2}$ built on the boundary layer momentum thickness δ_2 at the leading edge of the cavity is relevant to describe the instability threshold of shear-layer oscillations (Rowley et al., 2002). Re_L is built on the cavity length and is used to predict the shear-layer excited frequencies, since this distance is used in the Rossiter's model (Rossiter, 1964). The third Reynolds number Re_D is built on the cavity depth and used for the centrifugal instability description (Brès & Colonius, 2008).

Flow instabilities can affect and lead to the destruction of a vortex. For example, wing tip vortices can develop Crow instabilities (Crow, 1970, Faure, 2008). The emergence of flow instabilities is also the origin of transition toward turbulence, like the hairpin vortical structures that develop on a wall boundary layer (Schlichting, 1960). In the present case of cavity flows, the centrifugal effects are the main cause of instability development. These centrifugal instabilities are of three types. Rotating flows between two cylinders develop Taylor-Couette instabilities: the streamlines are loops and this case corresponds to a closed system. Curvature effects imposed by wall lead to the development of Görtler instabilities, in that case, the streamlines are not closed and the system is said open. In the case of curvature effects with an external pressure gradient, a Dean instability can be found, which is also an open system (Mutabazi et al., 1990). Cavity flows induced by the development of a shear-layer are both closed and open systems because the streamlines are quasi-circular but they originate from the oscillations of the shear-layer. The cavity flow is governed by the linearized Navier-Stokes equations and can be investigated with a global stability analysis. A base flow is said to be asymptotically stable if the modulus of any initial perturbation tends to zero for large times otherwise it is asymptotically unstable (Schmid, 2007). The stability of a base flow is reduced to an eigenvalues problem. The associated eigenvectors are the physical global modes. If at least one of the eigenvalues has a positive real part, the base flow is asymptotically unstable and the instability is called a modal instability. If all of the eigenvalues have negative real parts, the global modes will eventually decay at large times, and the base-flow is asymptotically stable (Sipp et al., 2010). That global stability approach has been used for the study of open cavity flows (Brès & Colonius, 2008, Barbagallo et al., 2009, Sipp et al., 2010, Meseguer-Garrido et al., 2011, de Vincente et al., 2014, Gomez et al., 2014, Yamouni et al., 2013, Meseguer-Garrido et al., 2014) and lid-driven cavity flows (Chicheportiche et al., 2008, Merle et al., 2010). That approach has demonstrated that both two-dimensional and three-dimensional cavity modes can coexist and are dependent on the cavity geometry and Reynolds number. It is particularly useful in order to elaborate flow control strategies (Sipp, 2012, Luchini & Bottaro, 2014). Most of the configurations studied corresponds to a cavity aspect ratio equals to one, except Meseguer-Garrido et al. (2014) who varied L/D between 1.2 and 3.

The objective of the study is to conduct PIV measurements in a cavity of modular dimensions. Velocity fields provide information on flow vortical features. Parametric analysis is conducted and compared with theoretical behavior of Taylor-Couette and Görtler flows, and experimental data for a lid-driven cavity flow.

2 Experimental set-up and apparatus

The experimental facility is a low-speed open-circuit wind tunnel (Faure et al. 2007, Faure et al. 2009, Basley et al. 2011, Douay et al. 2013). The cavity dimensions (length L, depth D and span S) can vary and different aspect ratios L/D between 0.5 and 2 are investigated. The cavity span is fixed and corresponds to the test section dimension and the origin of the coordinate system is placed at the cavity leading edge at mid-span. The maximum turbulence intensity in the external flow is less 1%. The Reynolds number Re_D is built on the cavity depth D. It has been shown that this Reynolds number is relevant for the internal cavity flow description (Brès & Colonius, 2008, Faure et al. 2009). PIV measurements are conducted with a pulsed YAG laser emitting a 0.25 mm thick light sheet at 532 nm with energy of 250 mJ per pulse. The frame series are recorded with a 10-bit camera at a frequency of 20 Hz with a resolution of 1032×778 pixels. Velocity fields are obtained with an optical flow algorithm using orthogonal dynamic programming (Quénot, 1992). This image processing method provides highly resolved fields (1 vector per pixel) and is particularly efficient for high velocity gradient regions, such as shear-layers or recirculations. The velocity resolution is 1 / 32nd pixel or a relative velocity accuracy of 0.15% (Faure et al. 2006). The velocity field is not time-resolved in the external flow and shear-layer, where oscillations are of the order of 20 Hz, but is time-resolved inside the cavity where lower velocities are found. Hereafter, results for two observation planes are presented: a (x,y) plane located at mid-span (z = 0), to get the main flow morphology of the recirculation (Figure 1-a) and a (x,z) plane, to describe the development of centrifugal instabilities superimposed upon this flow (Figure 1-b). For each of these configurations, the camera gets a sight of the whole cavity along its length or its span with a magnification of 2×10^{-4} m/pixel. In the first configuration, the (x,y) plane is located at the cavity mid-span. In the second configuration, the (x,z) plane is placed at a relative vertical position y / D = –0.3. For the first measurement configuration, the time interval between to laser flashes is calculated in order to get a maximum displacement of images of particles equals to 10 pixels inside the cavity. This setting gives larger displacements in the external flow but thanks to the optical flow algorithm, resolves both the cavity flow and the external flow. For the second measurement configuration, the time interval is the same as the camera and we get time-resolved velocity fields, as the laser sheet is completely immersed inside the cavity, and velocities are at least 10 times lower than the external flow.

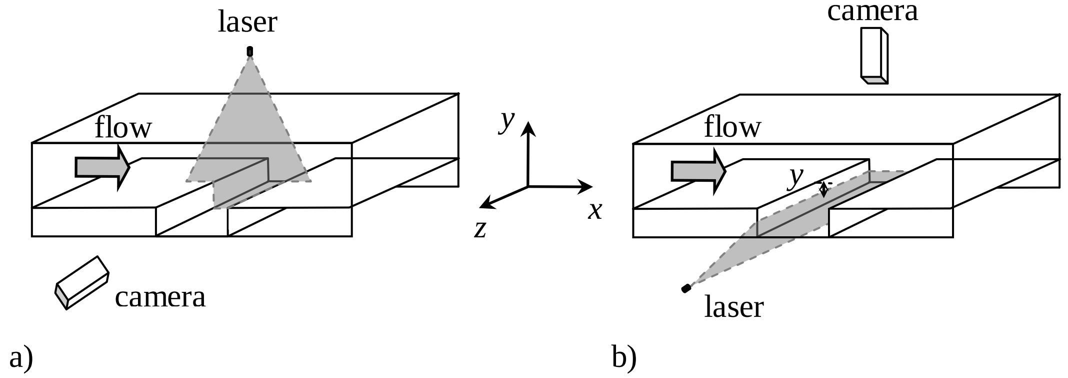

Figure 1: Flow visualizations a) in a (x,y) plane or b) in a (x,z) plane inside the cavity.

3 PIV velocity field

Before computing velocity fields from a PIV sequence, the background noise of the recorded frames is filtered by the subtraction of a reference frame, recorded with no flow (Faure et al. 2006). In addition, the regions of the frame situated outside the flow are masked. As the tracers have different diameters and are not scattering the same amount of light, a high-pass filter is finally applied to uniform the size of each particle image and for compensation of illumination changes. The Reynolds decomposition of velocity between an averaged velocity and a time-dependant fluctuation is applied on each component. A convergence study inside the cavity shows that, in the range of Reynolds number under consideration, the mean and second order moments of velocity are converged averaging 600 fields with a relative accuracy within 1%.

3.1 Mean velocity

The three-dimensional character of the cavity flow has been recognized in previous studies (Faure et al., 2007, Brès & Colonius, 2008, Faure et al., 2009). This is resulting from the cavity flow instability (Douay, 2014). However some comparisons of the present cavity geometry with two-dimensional analysis can be realized around the cavity symmetry plane (figure 18 in Brès & Colonius, 2008). The averaged streamlines are given in a (x,y) plane for four aspect ratios in Figure 2. Because of high density of velocity vectors given by the PIV optical flow technique, only one streamline out of ten is plotted to keep the figure clear. Note that flow morphology in that plane is almost independent of Reynolds number, so we present results only for Re_D = 4230. The cavity flow is marked by a recirculation characterized by a vortex of spanwise axis and located near the downstream cavity wall. According to the aspect ratio variation, the flow exhibits one vortex for L/D =1, 1.5 and 2 (Figure 2-b,c,d). This primary vortex is confined to the downstream cavity wall and a secondary counter-rotating vortex appears near the bottom of the upstream cavity wall for L/D = 1.5 and 2 (Figure 2-c,d). For L/D = 0.5 the primary vortex is placed in the upper half of the cavity depth while the secondary vortex is below (Figure 2-a). That analysis confirms previous flow visualizations conducted in the same experimental set-up (Faure et al., 2009, Faure et al., 2007). As the streamlines are closed, the center of the recirculation is easily identified.

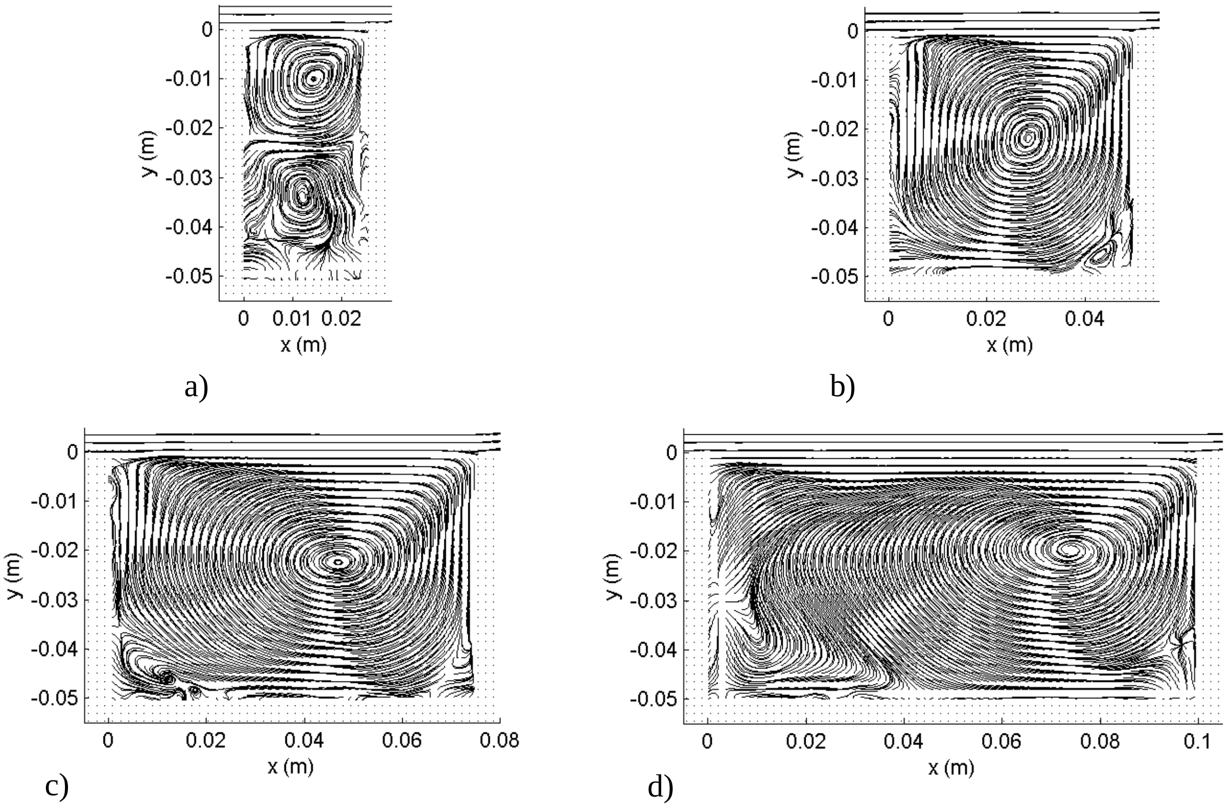

Figure 2: Average streamlines of the cavity flow for Re_D = 4230 and a) L/D = 0.5, b) L/D = 1, c) L/D = 1.5, d) L/D = 2.

The dimensionless mean velocity is shown in Figure 3 for $L/D = 0.5$ and $Re_D = 4230$. In order to get a readable view of the cavity flow with small velocity, the color scale is saturated, so the external flow appears as a dark red stripe. The mean axial velocity presents a positive region at the bottom of the cavity and a negative region at its mid-depth (Figure 3-a), while the vertical velocity shows a positive region near the upstream wall and a negative region near the downstream wall (Figure 3-b), evidence of a rotating flow confirmed by the modulus (Figure 3-c). Note that the lower counter-rotating vortex identified in streamlines, is invisible in these figures because of its very low velocity amplitude. Similar comments can be done for $L/D = 1$, the recirculation vortex spreading along the cavity length and depth (Figure 4). Note the streamlines (Figure 2-b) and x component of velocity (Figure 4-a) which are in a very good agreement with the two-dimensional base flow results of Citro et al. (2014), for $L/D = 1$ and base flow Reynolds numbers $Re_{BF} = 1370$ and 4140. This indicates that the average velocity field in the present study is not far from a base flow, in a sense of a global stability analysis. Furthermore, the instability is weak, and does not much alter the streamlines that exist in sub-critical flow past the bifurcation, as it can be seen from the comparison between the averaged and instantaneous fields (Douay et al. 2013). For $L/D = 1.5$ (Figure 5), the same global morphology is found, with an increase in velocity magnitude inside the cavity due to a stronger injection from the developing shear-layer oscillations. The same comment is valid for $L/D = 2$ (Figure 6), the recirculation primary vortex is not extending towards the leading cavity wall and its upstream part is blurred because of its time-dependence and the average effect. The small relative positive and negative regions measured inside the cavity near the edge and the bottom of the upstream wall are resulting of laser reflections and are not physical.

Velocity profiles inside the cavity are plotted, for comparisons with other results, on different lines for constant x values, for the mean relative x and y components (Figure 7, Figure 8). For each aspect ratio L/D, the first and last profiles are obtained at 2 mm from the vertical cavity walls and the other two profiles are distributed in order to get uniform intervals between these abscissa. For $L/D = 0.5$ the primary vortex is limited to the upper half of the cavity, since both the axial and vertical velocity components are equal to zero for $y < -0.03$ m. Apart from the walls vicinity, for -0.01 m $< y < -0.03$ m, there is a negative x component velocity (Figure 7-a) and the y component changes its sign at mid-cavity length (Figure 8-a), which characterizes a plunging or rising flow. For $L/D = 1$ the vortex spreads on the cavity depth (Figure 7-b) and the y component of velocity still shows a plunging flow near the downstream cavity wall (Figure 8-b). The same flow development is found for $L/D = 1.5$ and 2, with an increase of the modulus of the minimum x or y velocity components.

The comparison of the present experimental cavity flow with the base flow obtained with a global stability analysis (Sipp & Lebedev, 2007) is conducted, for the only geometrical configuration documented and corresponding to $L/D = 1$, in the middle of the cavity length (Figure 9). A good agreement is found between the velocity profiles. In this figure, the relative vertical distance inside the cavity is obtained dividing y by the cavity depth D. The cavity velocity is normalized with the cavity velocity U_b, obtained by fitting the measured minimum with the base flow obtained by Sipp & Lebedev. It is found $U_b = 0.41\ \mathrm{m{\cdot}s^{-1}}$ corresponding to a Reynolds number $Re_b = U_b\, D\,/\,\nu = 1366$, which is not far from critical Reynolds number value of 1370 found in Citro et al. (2014). Thus we can say that the relevant velocity scale inside the cavity is the velocity U_b which is proportional to the external flow velocity, confirming previous observations (Faure et al. 2007).

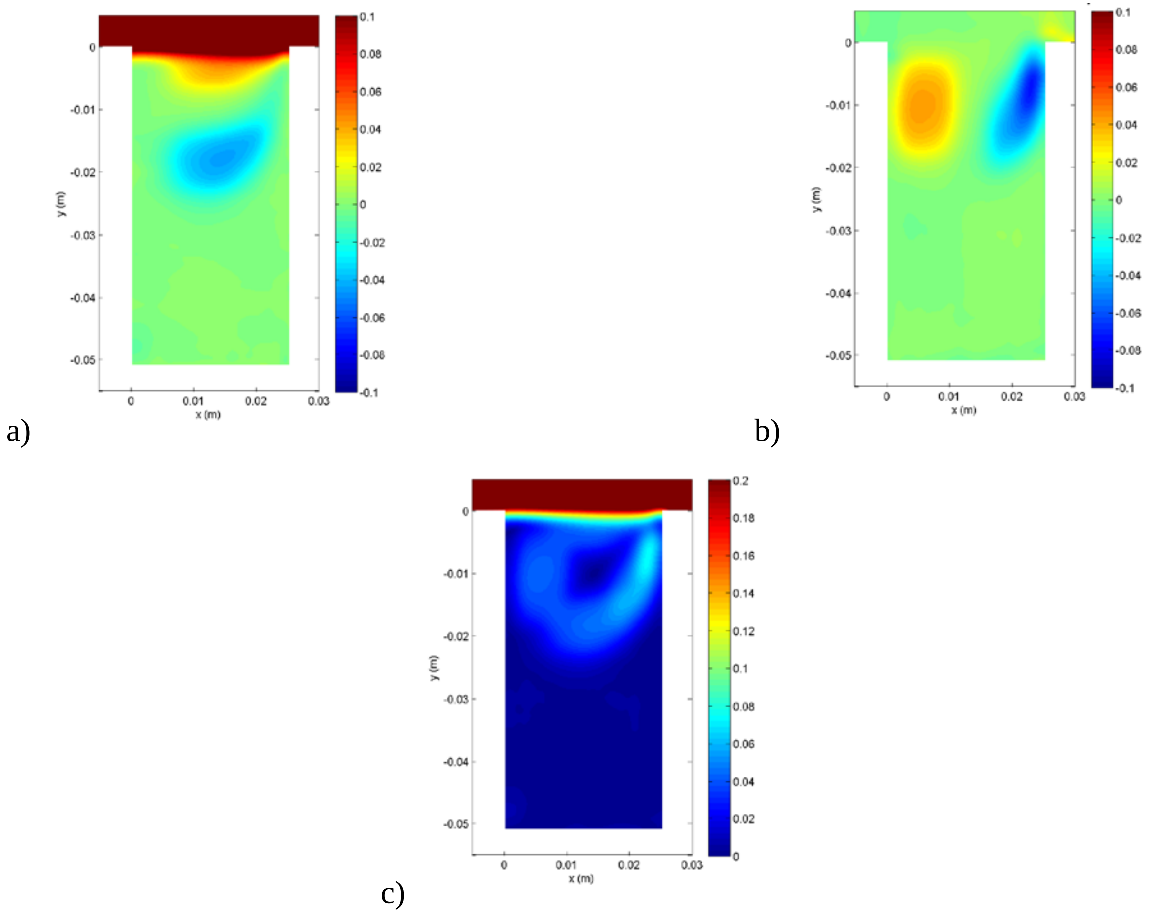

Figure 3: Mean velocity for Re_D = 4230 and L/D = 0.5 a) relative x component $\overline{U}_x/U_e$, b) relative y component $\overline{U}_y/U_e$, c) relative velocity modulus $\overline{U}/U_e$.

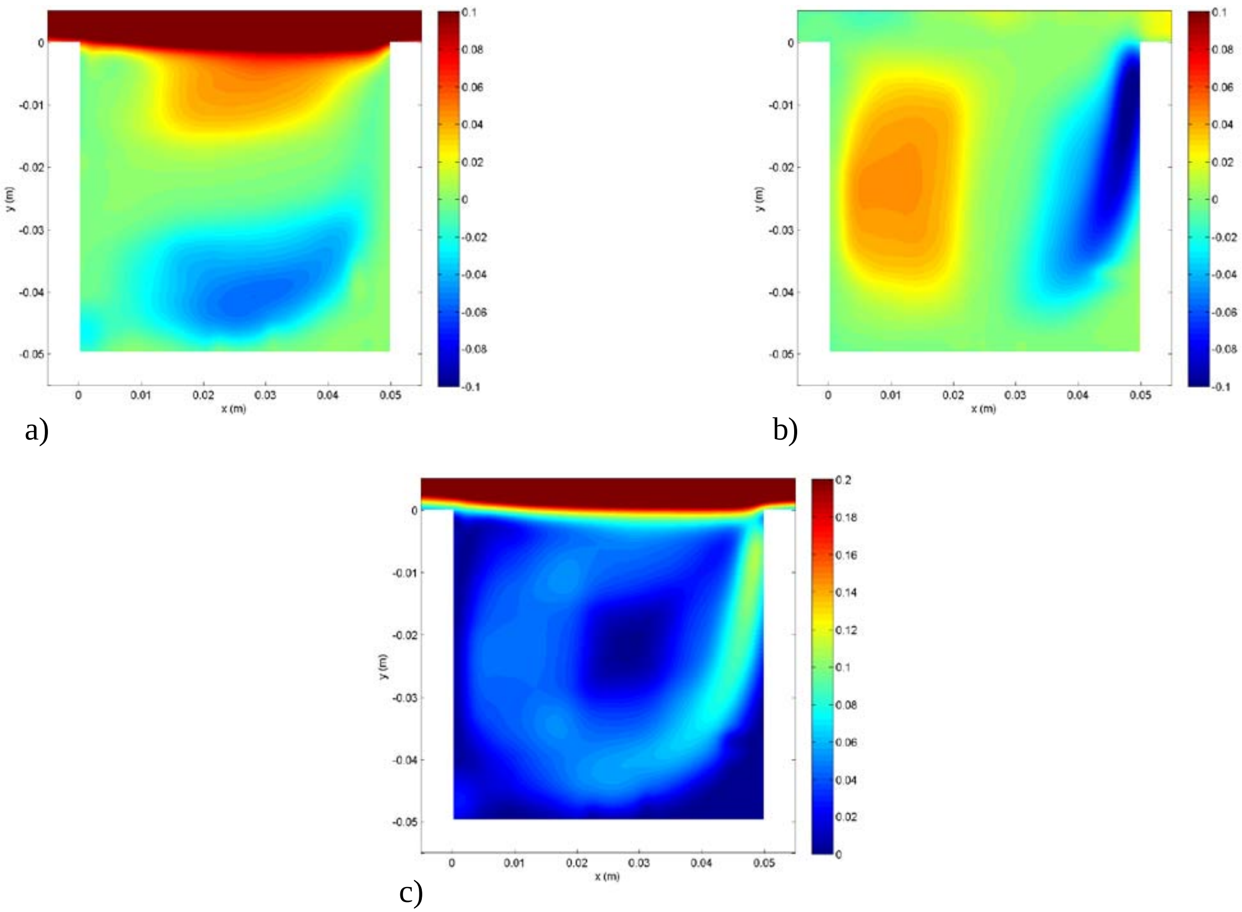

Figure 4: Mean velocity for Re_D = 4230 and L/D = 1 a) relative x component $\overline{U}_x / U_e$, b) relative y component $\overline{U}_y / U_e$, c) relative velocity modulus $\overline{U} / U_e$.

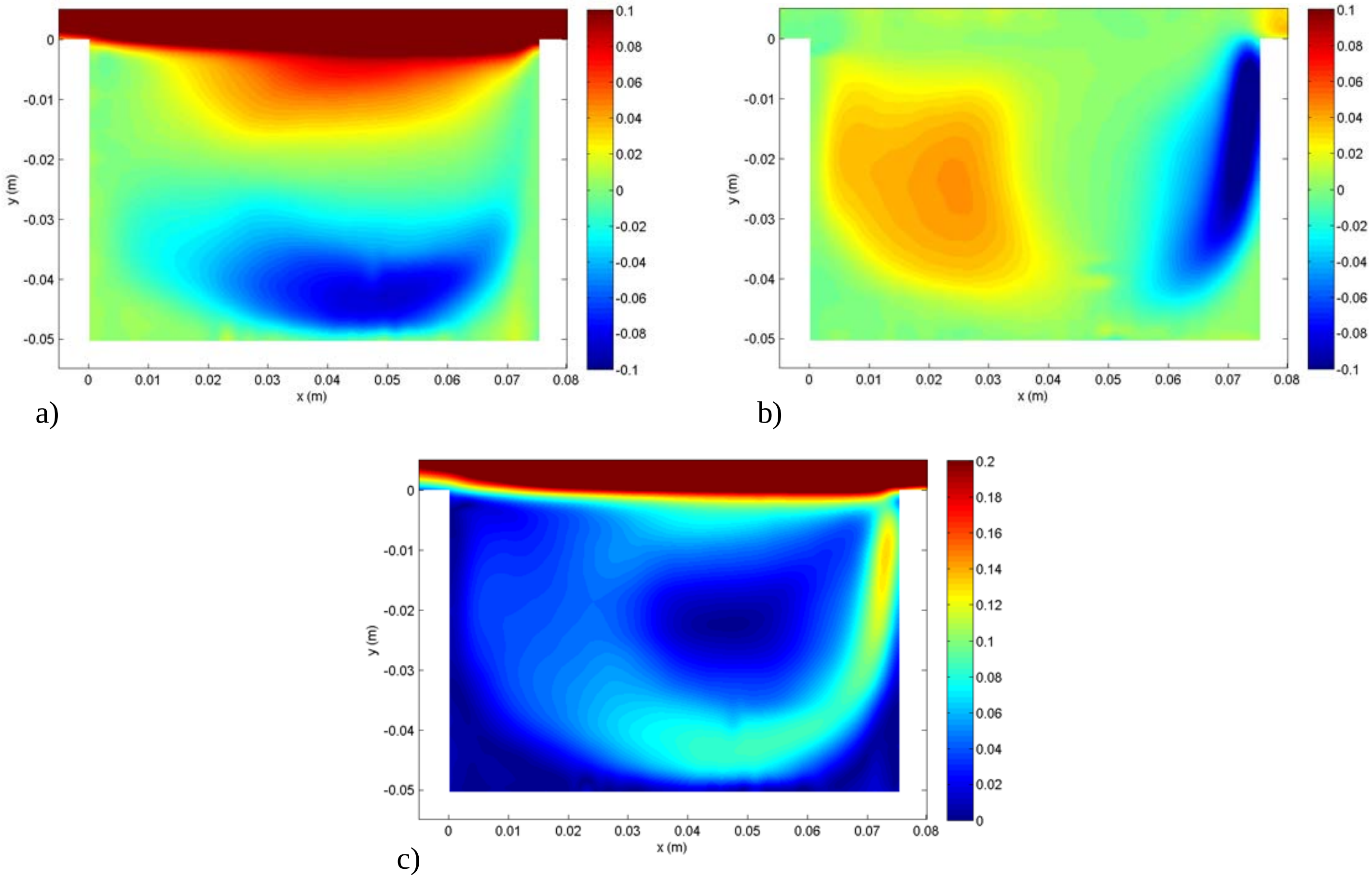

Figure 5: Mean velocity for Re_D = 4230 and L/D = 1.5 a) relative x component $\overline{U}_x / U_e$, b) relative y component $\overline{U}_y / U_e$, c) relative velocity modulus $\overline{U} / U_e$.

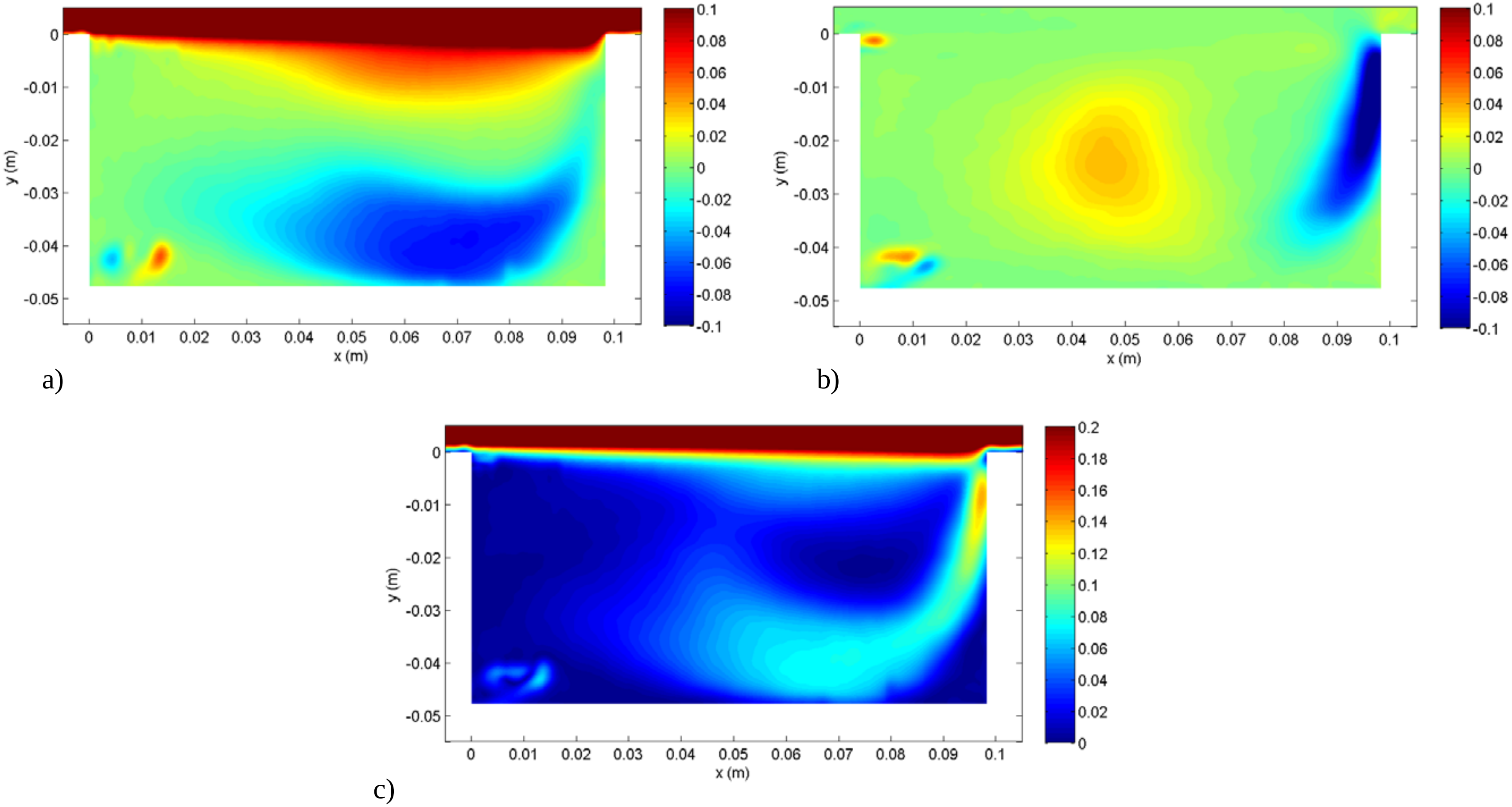

Figure 6: Mean velocity for Re_D = 4230 and L/D = 2 a) relative x component $\overline{U}_x / U_e$, b) relative y component $\overline{U}_y / U_e$, c) relative velocity modulus $\overline{U} / U_e$.

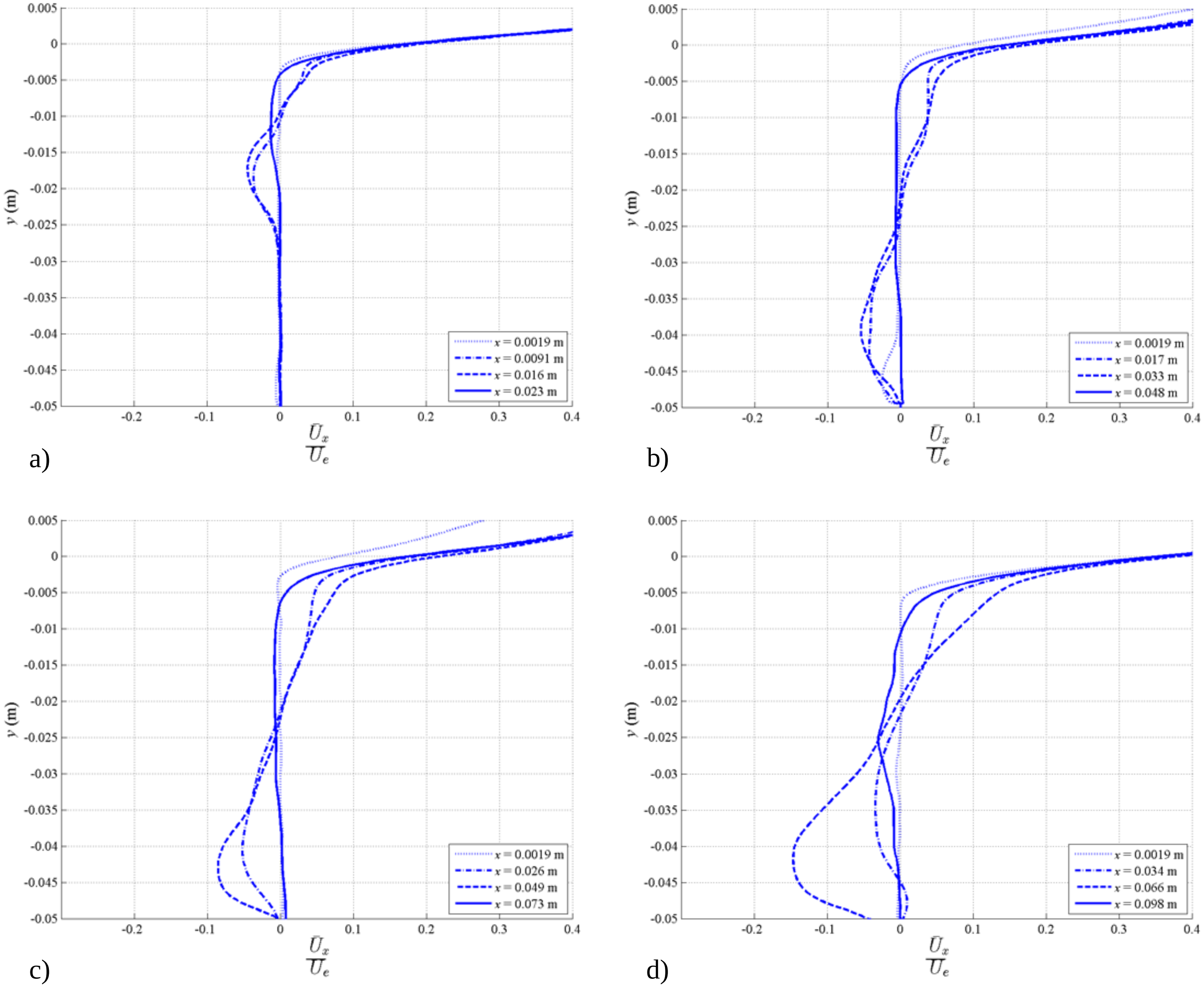

Figure 7: Relative x component of mean velocity $\overline{U}_x / U_e$ profiles for different positions, Re_D = 4230 and a) L/D = 0.5, b) L/D = 1, c) L/D = 1.5, d) L/D = 2.

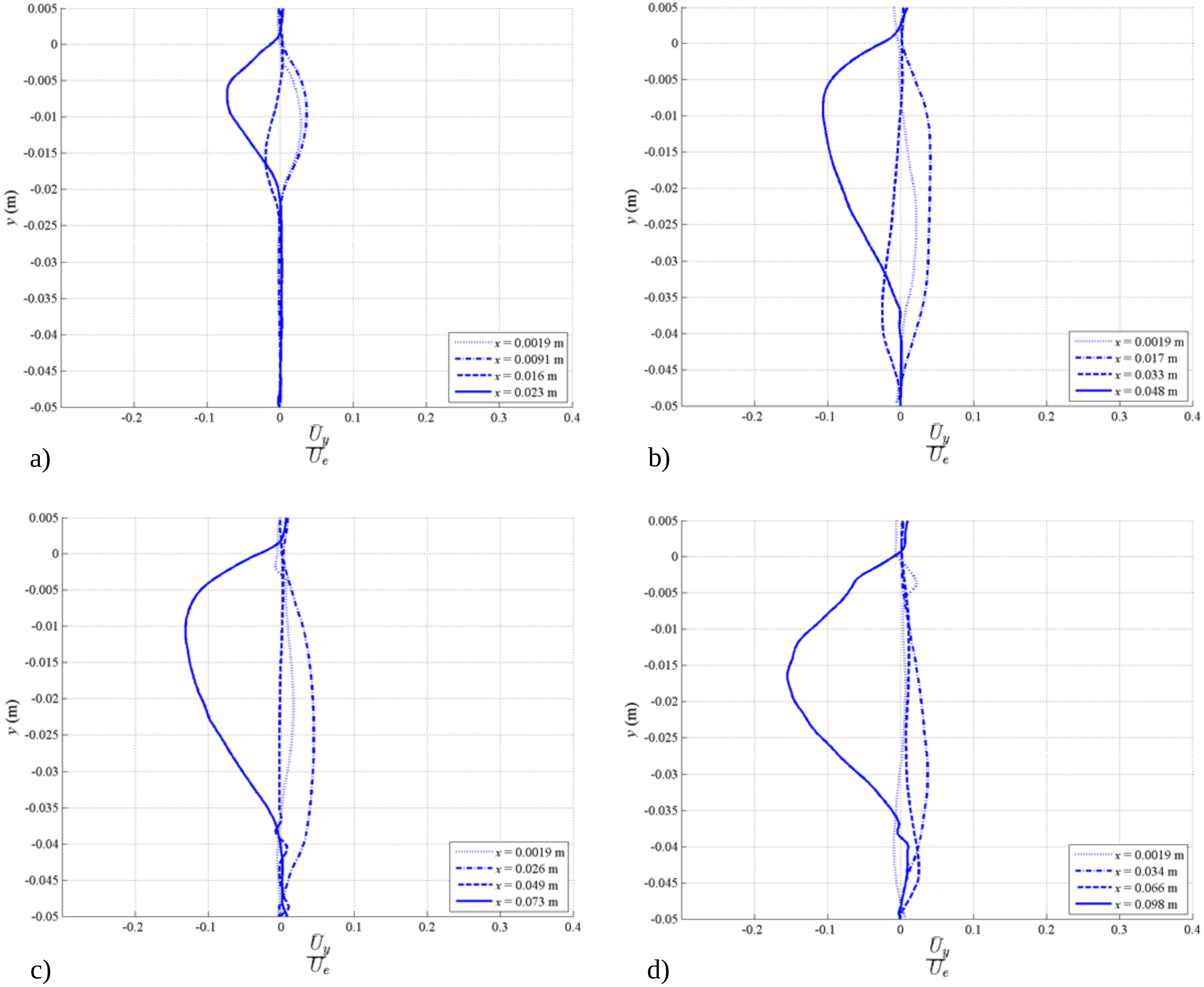

Figure 8: Relative y component of mean velocity $\overline{U}_y / U_e$ profiles for different positions, Re_D = 4230 and a) L/D = 0.5, b) L/D = 1, c) L/D = 1.5, d) L/D = 2.

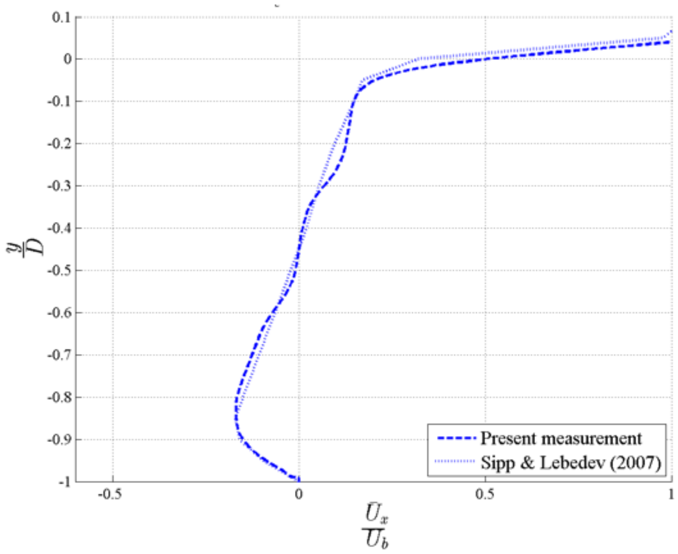

Figure 9: Comparison between the longitudinal velocity for Re_D = 4230 and L/D = 1 at the relative abscissa x/D = 0.5 obtained in the present cavity flow and by Sipp & Lebedev (2007) for Re_b = 4140 and L/D = 1.

3.2 Turbulence stress

Upstream of the cavity and for Re_D = 4230, the measured boundary layer displacement thickness and momentum thickness are respectively δ_1 = 2.65 mm and δ_2 = 1.23 mm. The shape factor $H = \delta_1 / \delta_2 = 2.16$, indicating that the boundary layer is not perfectly laminar. For the same Reynolds number, the turbulence inside the cavity increases with aspect ratio L/D. For L/D = 2, we note that the maximum turbulence intensity inside the cavity is 7%, and it is located in a region near the downstream cavity edge where the shear-layer impinges (Figure 10). The turbulence intensity distribution is not equivalent for the *x* and *y* components. Standard deviation of velocity fluctuations along the *x*-axis shows a structure in two lobes distributed on both sides of the cavity top-plane while the standard deviation of the *y*-axis fluctuations exhibits a unique lobe centered on the same position. The shear stress shows that the fluctuation along the *x* and *y*-axis are opposite signs above, and of the same sign below the cavity top-plane. Similar organization was previously observed (Kuo & Huang, 2001, Basley et al. 2011). The large levels measured inside the cavity near the upstream wall are resulting of laser reflections and are not physical.

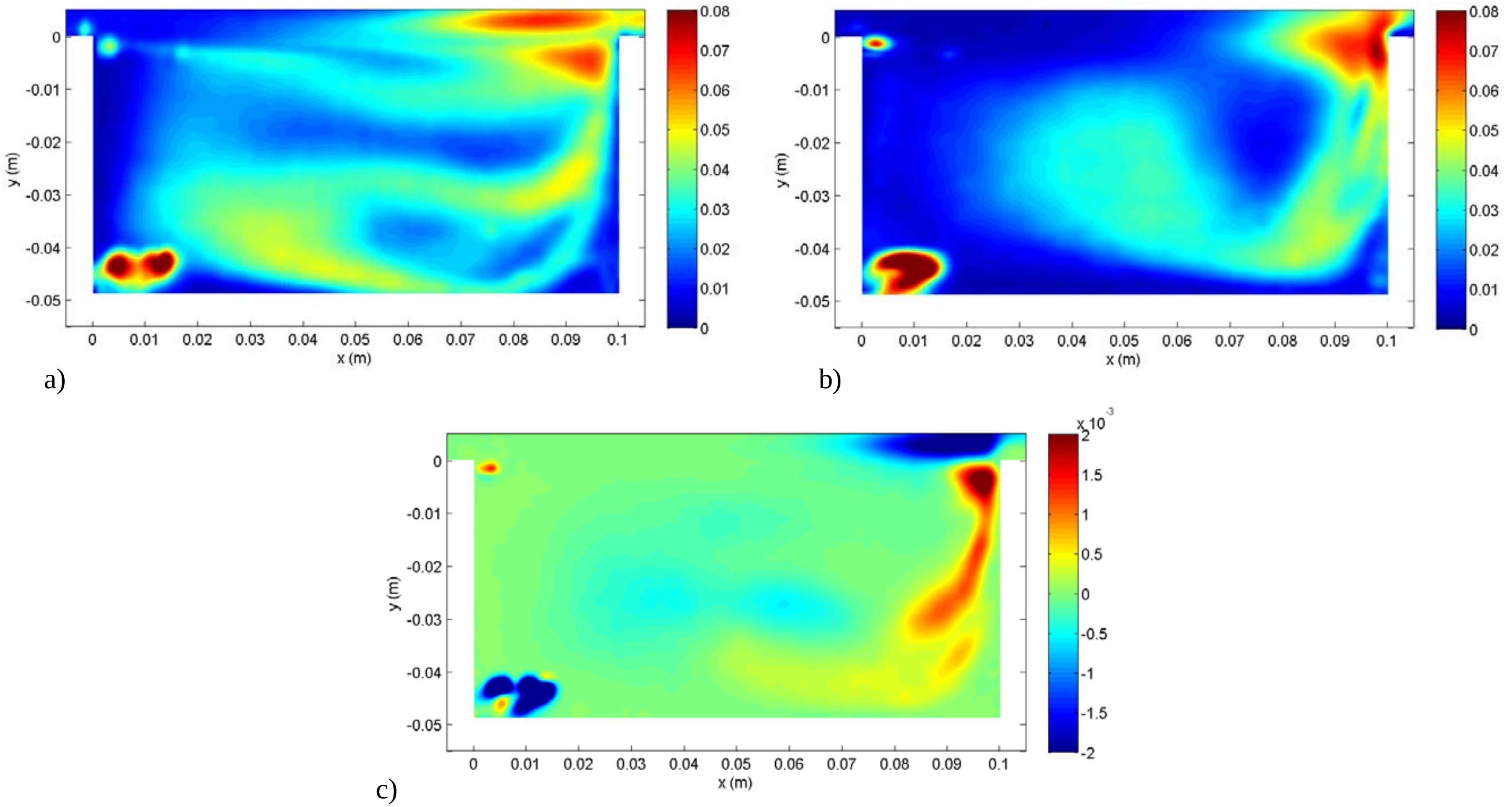

Figure 10: Reynolds stress tensor for $Re_D = 4230$ and $L/D = 2$ a) relative rms value of the x component $\sqrt{\overline{u_x^2}}/U_e$, b) relative rms value of the y component $\sqrt{\overline{u_y^2}}/U_e$, c) relative covariance of the x y component $\overline{u_x u_y}/U_e^2$.

4 Parametric analysis

4.1 Development of instability

As previously mentioned, for any aspect ratio *L/D*, the flow within the cavity is driven by a primary vortex of spanwise axis. For particular flow conditions, vortices resulting from the centrifugal instability develop along the span. They have been observed on flow visualizations (Faure et al., 2007, Faure et al., 2009) and PIV measurements (Faure et al., 2008). Two-component PIV fields in the (x,z) plane are carried out with a large velocity component perpendicular to the measurement plane and are subject to measuring noise because the magnitude of the velocity modulation caused by these vortices is weak. In order to identify centrifugal vortices, different detection criteria are applied to an instantaneous velocity field.

The vorticity is defined for a 2D velocity field as:

$$\Omega_z = \frac{\partial U_y}{\partial x} - \frac{\partial U_x}{\partial y} \tag{1}$$

The Q criterion is the second invariant of the velocity gradient tensor (Hunt et al. 1988). For a 2D velocity field, its expression is:

$$Q = -\frac{1}{2}\left[\left(\frac{\partial \overline{U}_x}{\partial x}\right)^2 + \left(\frac{\partial \overline{U}_y}{\partial y}\right)^2 + \frac{\partial \overline{U}_x}{\partial y}\frac{\partial \overline{U}_y}{\partial x}\right] \tag{2}$$

The region $Q > 0$ defines the inner part of a vortex.

The λ_2 criterion is the second real eigenvalue of the tensor $T^2 + \Omega^2$, where T is the strain tensor and Ω the rotation tensor (Jeong & Hussein 1995):

$$\lambda_2 = \frac{\partial \overline{U}_x}{\partial y}\frac{\partial \overline{U}_y}{\partial x} - \frac{\partial \overline{U}_x}{\partial x}\frac{\partial \overline{U}_y}{\partial y} \tag{3}$$

$\lambda_2 < 0$ defines a minimum pressure region, which is a probable vortical region.

The Γ_2 criterion (Graftieaux et al., 2001, Michard & Favelier, 2004) is a normalized kinetic moment considering the relative motion around a particular point, it is defined by:

$$\Gamma_2(\vec{x}) = \frac{1}{A}\int_{\vec{x}'\in A} \frac{(\vec{x}'-\vec{x})\times\left[\vec{U}(\vec{x}')-\vec{U}(\vec{x})\right]}{\|\vec{x}'-\vec{x}\|\left\|\vec{U}(\vec{x}')-\vec{U}(\vec{x})\right\|}\,d\vec{x}' = \frac{1}{A}\int_{\vec{x}'\in A} \sin\varphi \, d\vec{x}' \tag{4}$$

A is a circle including the observation point $\vec{x}$ and φ is the angle made by the two vectors in the cross product. The function is not sensitive on the radius R of the circle A and in the present study this radius equals the distance between two vectors in the velocity field (Figure 11). Note that this criterion is Galilean invariant and can be applied when a vortex is advected by a mean flow. Then, Γ_2 ranges between -1 and 1 and reaches its maximum value at the center of a vortex.

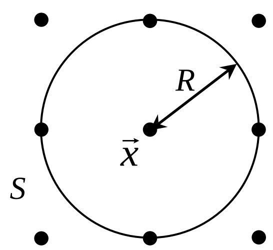

Figure 11: PIV grid and circle A for Γ_2 calculation.

The comparison between the four criteria previously defined is presented Figure 12 on an instantaneous field. The vorticity shows high levels in the instability rows present near the upstream cavity edge (Figure 12-a). Q and λ_2 criteria get also high values in these regions but fail to clearly identify each individual eddy (Figure 12-b,c). However, the vortical flow instabilities are well described with the Γ_2 criterion despite the strong velocity component orthogonal to the measurement plane (Figure 12-d). Thus, this latter seems to be a relevant filter for noised measurements. Note that Γ_2 criterion allows seeing the part of the raw of vortices orthogonal to the plane near the upstream cavity edge, but also the part of vortices parallel to the plane, in the center of Figure 12 between 0.02 m $\leq x \leq$ 0.06 m.

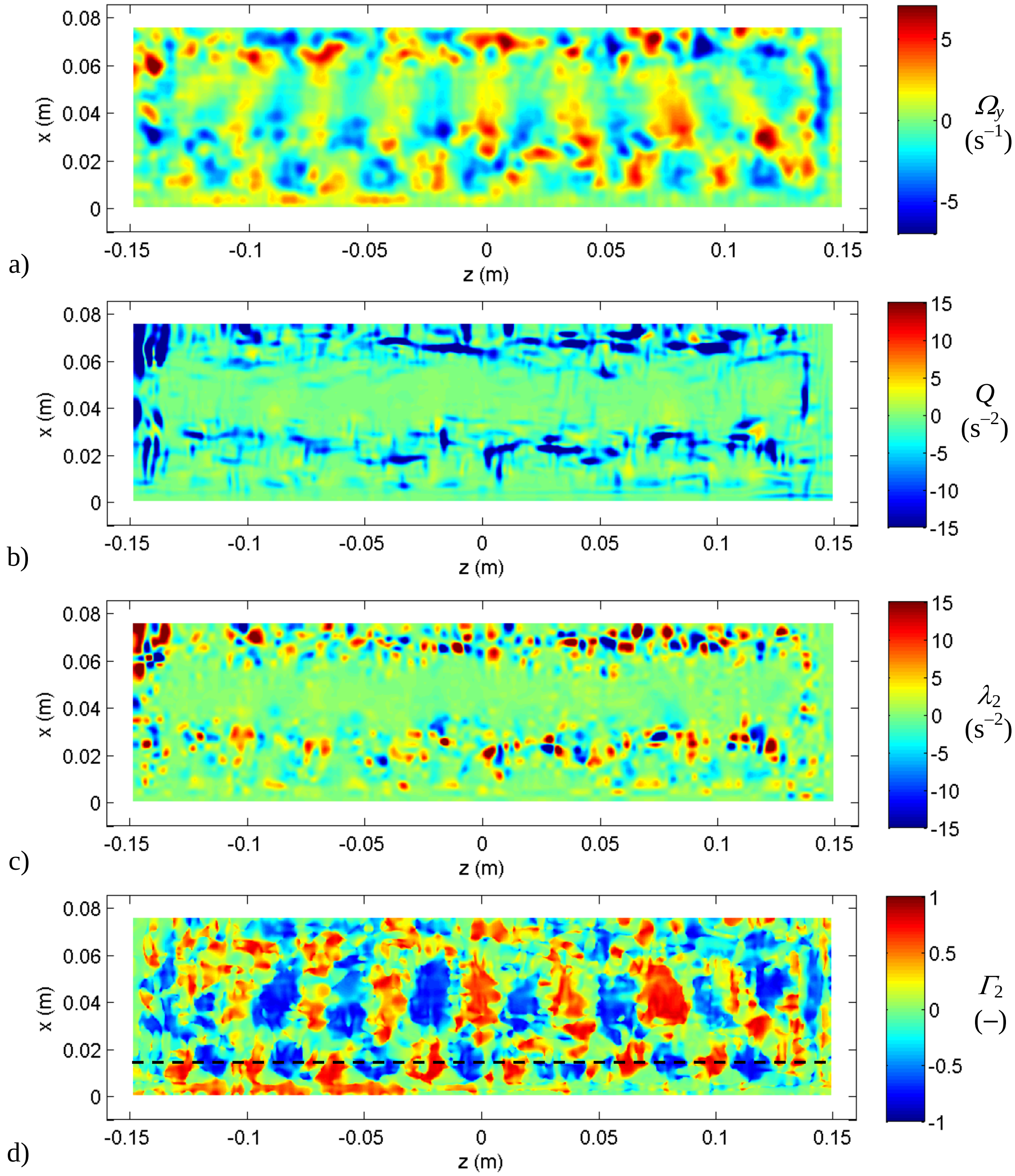

Figure 12: Vortex detection criteria on an instantaneous field for Re_D = 2300 and L/D = 1.5 in a (x, z) plane: a) vorticity Ω_z, b) Q criterion, c) λ_2 criterion, d) Γ_2 criterion.

From the identification of vortical flow structures on every PIV sequence, a single line is extracted from each Γ_2 field (black dashed line in Figure 12) and allows building a space-time diagram (Figure 13). On such a diagram, vertical patterns are associated with stationary vortices while oblique lines are associated with traveling patterns. The lateral drift of the pairs of vortices to the lateral cavity walls is observed. This drift confirms that the influence of the vortices does not alter much the averaged velocity flow field, which can be consider as a base flow. It is then possible to measure a transverse drift velocity W_s from the maximum slope of equal values in this diagram, and their wavelength λ.

These results are compared with the analysis of flow visualizations (Faure et al., 2009). A good agreement is found between this method and flow visualization for the drift velocity W_s (Figure 14), the dispersion between measurements is the order in magnitude of the uncertainty errors. The general behavior is a global arrangement of W_s / U_e with *L/D*, and a low decrease with Reynolds number, followed by an increase for $Re_D > 6000$. Centrifugal instabilities develop along the cavity span, so their number is strongly tied to their wavelength. However, the pairs of vortices are not always adjoined, so the measurement of an average wavelength seems relevant (Figure 15). The general trend is an increase of the wavelength with aspect ratio *L/D*. The instability generation is driven by a three-dimensional coupling between the axial and span directions (Neary & Stephanoff, 1987). Again, these results corroborate flow visualizations.

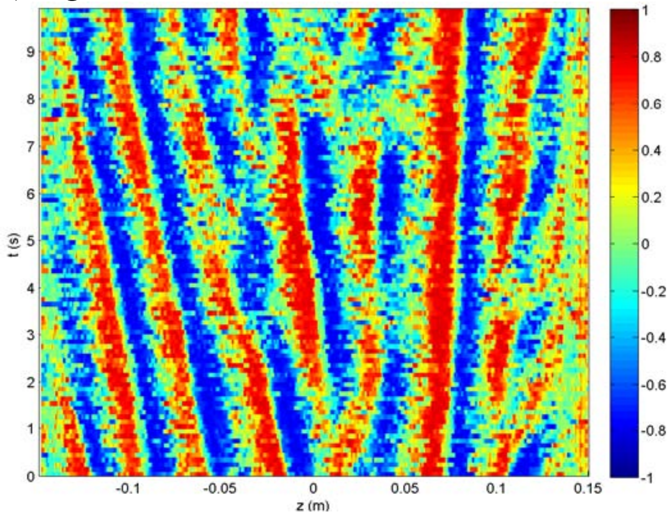

Figure 13: Space-time diagram of the Γ_2 criterion for L/D = 1.5and Re_D = 2300.

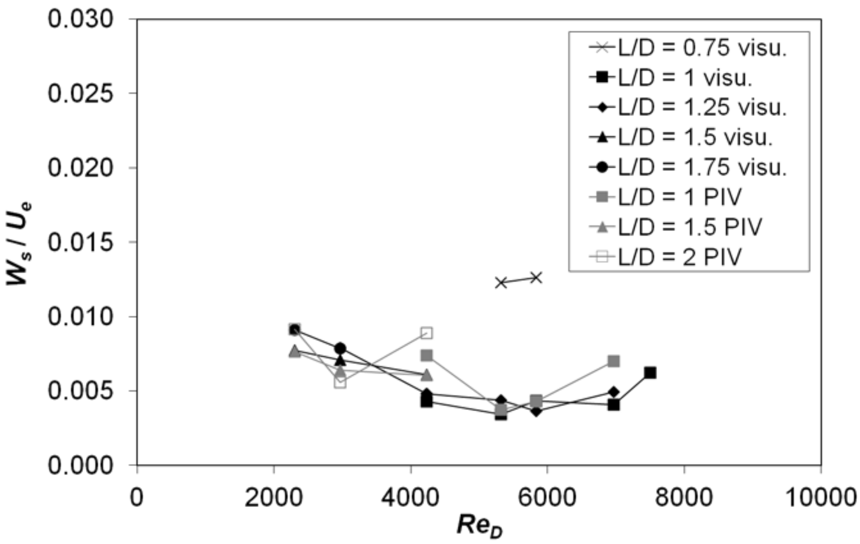

Figure 14: Drift velocity W_s of centrifugal instabilities: comparison between PIV measurements (gray symbols) and flow visualizations (black symbols).

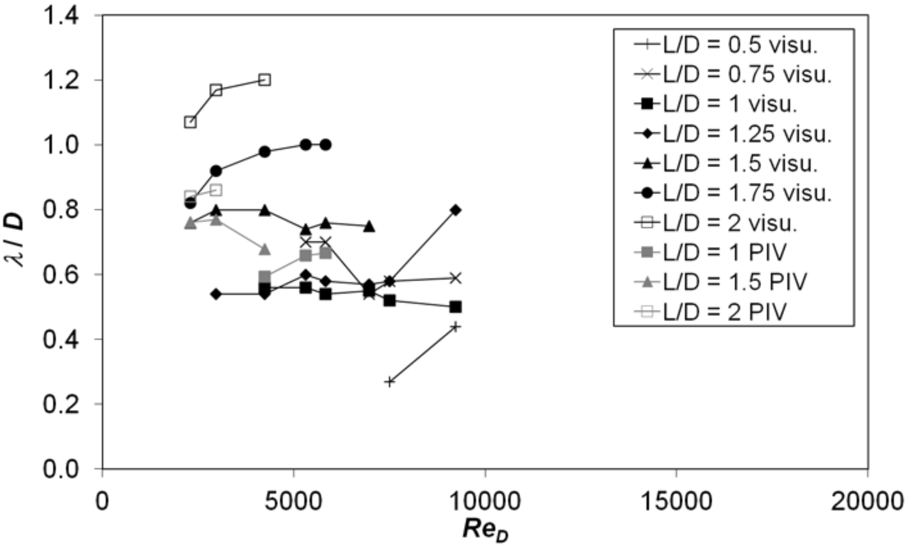

Figure 15: Relative wavelength λ / D of centrifugal instabilities: comparison between PIV measurements (gray symbols) and flow visualizations (black symbols).

4.2 Rayleigh discriminant

The following discussion addresses the origin and development of three-dimensional instability observed in the previous section. It is assumed to be associated with the closed streamlines in the cavity recirculation (Brès & Colonius, 2008). That analysis was previously conducted on numerical simulations of a backward-facing step (Barkley et al., 2002) and cavity flow (Brès & Colonius, 2008). In order to get a stability criterion from experimental data, we consider the averaged velocity field as a base state. The centrifugal instability issue was considered by Rayleigh (1916), showing that instability may arise in a flow with closed streamlines if there is an outward decrease in the magnitude of the angular momentum. The Rayleigh discriminant is defined as:

$$\eta(x,y) = -\frac{\partial \left\| \vec{r}(x,y) \times \vec{\bar{U}}(x,y) \right\|^2}{\partial r} \tag{5}$$

where $\vec{r}(x,y)$ is the radial coordinate from the center (x_c, y_c) of the recirculation vortex. This center is easily measured from the closed streamlines of PIV time-averaged velocity fields (Figure 2). Although that position is accurately derived from velocity fields, the Rayleigh discriminant is weakly dependent on its value (Brès & Colonius, 2008). Thus, a viscous flow is stable if $\eta < 0$ and potentially unstable if $\eta > 0$. Results are given from fields obtained in a (x,y) plane at midspan inside the cavity, for $Re_D = 4230$ for aspect ratios L/D from 0.5 to 2 with the same color scale for comparison (Figure 16). The external flow and its injection inside the cavity are stable regions. In any case, the region of maximum potentially unstable flow is the external part of the recirculation vortex, where the velocity decays with the radius from the center. The inner part of the recirculating vortex is stable and corresponds to the region where the velocity exhibits a solid-body rotation velocity profile (Chatellier et al., 2004) while the outer region shows an azimutal velocity decreasing as $1 / r$. For $L/D = 2$ (Figure 16-d) the boundary of the potentially unstable region is a little blurred in the upstream part of the cavity, because of the time dependance of the recirculation vortex near the upstream cavity edge. Note for $L/D = 0.5$ (Figure 16-a), that the potentially unstable region is mainly identified in the outer part of the upper vortex which presents the higher levels. Another observation is the increase of the maximum value of η

with L/D keeping Re_D constant. That result is predictable since we notice the increase of the recirculation strength and turbulence levels when L/D is increased.

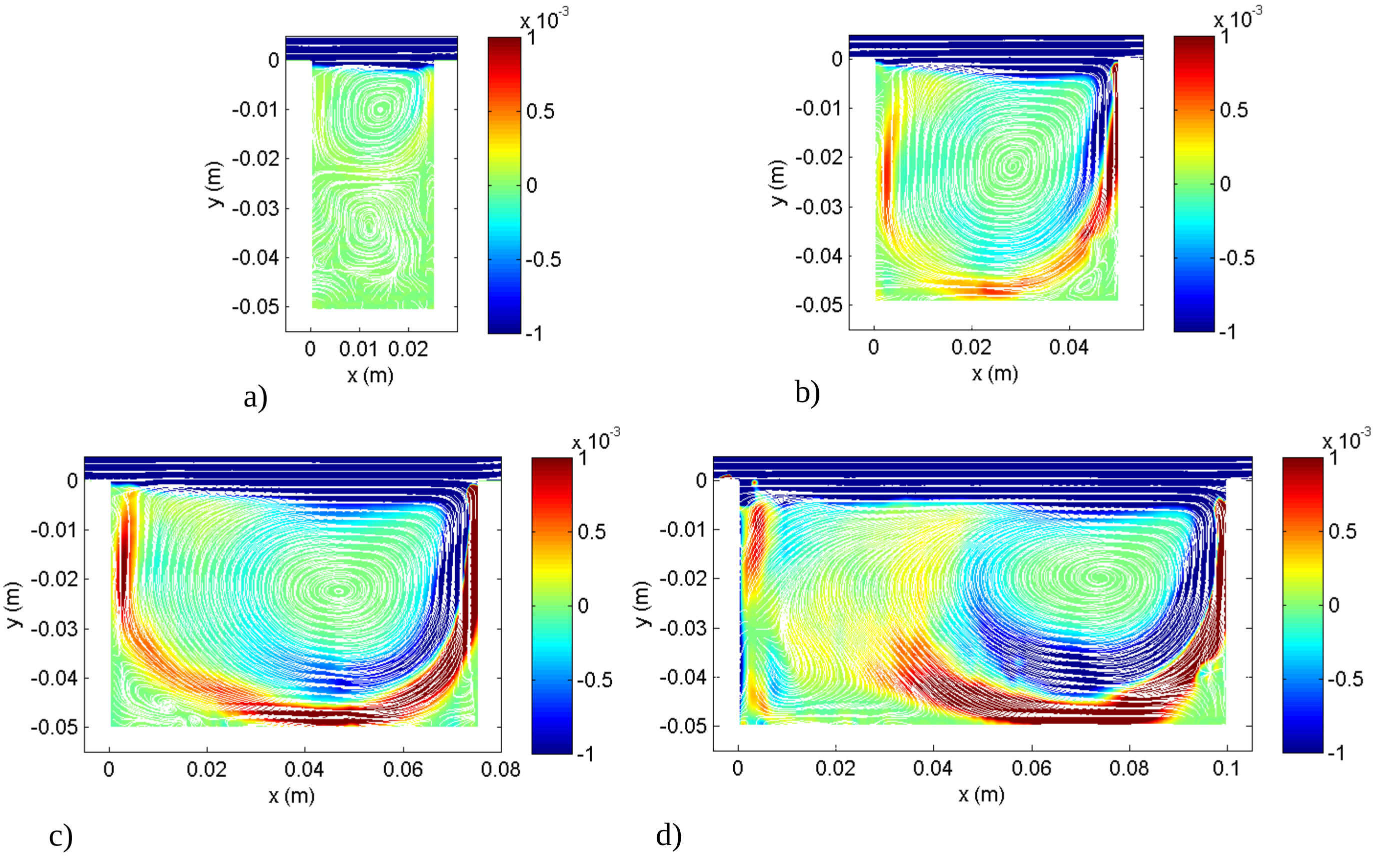

Figure 16: Rayleigh discriminant superimposed on averaged flow streamlines for Re_D = 4230 and a) L/D = 2, b) L/D = 1.5, c) L/D = 1, and d) L/D = 0.5.

In order to catch the development of centrifugal instability with flow parameters L/D and Re_D, it is necessary to get a unique value representing the unstable level inside the recirculation. The following comments can be drawn on the average of the positive values of Rayleigh discriminant inside the cavity η_{ave}:

- for $L/D = 0.5$, two recirculation vortices are present along the cavity depth, the flow curvature radius is of the order of $L = D/2$, and the threshold for the observation of centrifugal instability is around $\eta_{ave}(x,y) = 1.6\times10^{-4}$ $m^3.s^{-2}$.
- for L/D = 1, 1.5 and 2, the recirculation vortex spreads along the whole cavity depth, the flow curvature radius is of the order of D, and the threshold for the observation of centrifugal instability shows a unique value around $\eta_{ave}(x,y) = 5.5\times10^{-5}$ $m^3.s^{-2}$.

If that value η_{ave} is divided by the maximum radial extension of the potentially unstable region inside the recirculation $d_{i,max}$, there is a unique threshold for the emergence of centrifugal instability and counter-rotating vortices (Figure 17). In addition, the comparison of $\eta_{ave} / d_{i,max}$ with flow visualizations (Faure et al., 2009) is provided in that figure, with white-filled symbols for absence of centrifugal instability, colored-filled symbol for the presence of centrifugal instability and gray-filled symbols for transitional flow. Note that, for a given L/D, values of $\eta_{ave} / d_{i,max}$ are increasing with Reynolds number, except for L/D = 0,5 where the transitional state is not reached for the larger value of Re_D investigated. The threshold for the emergence of centrifugal instability is found around $\eta_{ave} / d_{i,max} = 8{,}7\times10^{-3}$ $m^2\cdot s^{-2}$.

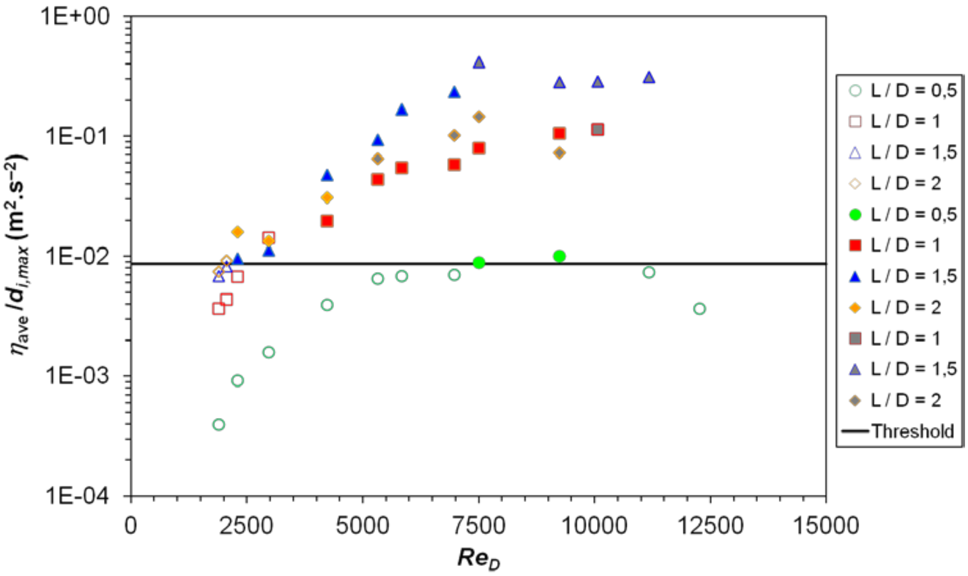

Figure 17: Average Rayleigh discriminant η_{ave} divided by the potentially unstable distance d_i inside the cavity versus Reynolds number Re_D , for $S/D = 6$, with the following notation convention: *white-filled symbols* no centrifugal instability, *colored-filled symbols* spanwise instability, *gray-filled symbols* transitional flow, *continuous line* observed threshold.

It has been demonstrated (Faure et al., 2009) that there is no influence of the span ratio on the appearance of centrifugal instability in the range $3 \leq S/D \leq 12$ (Figure 18). The data for which the centrifugal instability is developed are in accordance with the only incompressible configuration studied by Brès & Colonius (2008) corresponding, for $Re_D > 1500$, to a case of 2D stable and 3D unstable flow. This experimental observation of the development of the centrifugal instability is strengthening the three dimensional nature of the flow previously mentioned. Therefore the flow dynamical properties inside the cavity can be reduced to two dimensionless numbers Re_D and L/D. However, a preliminary study for $S/D = 12$ shows that the threshold for the occurrence of centrifugal instability is around $\eta_{ave} / d_{i,max} = 5\times10^{-3}$ $m^2{\cdot}s^{-2}$ for $Re_D = 2130$. Thus, the recirculation curvature radius may be not the only parameter that drives the centrifugal instability. Lateral confinement should also play a role since there might be a lower threshold when the lateral wall influence is lowered. The increase of S/D and the invariance of the development of centrifugal instability, in terms of critical values for Re_D and L/D, should be linked with a decrease of the threshold for $\eta_{ave} / d_{i,max}$. The higher value of the threshold $\eta_{ave} / d_{i,max}$ for $S/D = 6$ should be related to a longer cavity mouth L and a larger development of the Kelvin-Helmholtz instability in the shear-layer. This latter result should confirm the conclusion that three-dimensionality is connected to centrifugal instability previously mentioned (Brès & Colonius, 2008).

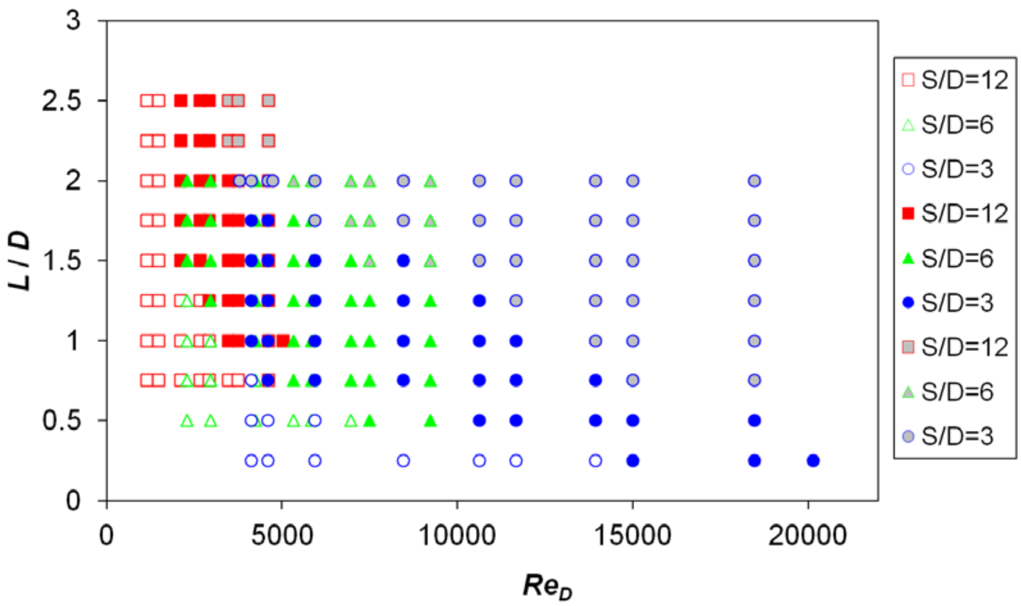

Figure 18: Existence diagram of centrifugal instability vortices versus Re_D for S/D = 12 (squares), S/D = 6 (triangles), S/D = 3 (circles) with the following notation conventions: *white-filled symbols* no centrifugal instability, *colored-filled symbols* spanwise instability, *gray-filled symbols* transitional flow (Faure et al., 2009).

4.3 Taylor-Couette analysis

It has been shown that the recirculation vortex presents two distinct regions from its center, an inner region of solid-body rotation and an outer region where the velocity decreases radially. We can wonder whether the instability is a Taylor-Couette instability, which is a peculiar type of centrifugal instability, considering the inner region as a rotating cylinder, the external cylinder being the cavity walls. Of course, that approach is only an indication, because considering the flow confined between two cylinders is a crude approximation of the recirculation inside the cavity. If a Reynolds number Re_Ω is defined from the rotational velocity Ω of the inner cylinder, Taylor-Couette instability develops beyond a critical Reynolds number $Re_{\Omega,c}$ (Tritton, 1988, Drazin & Reid, 1981), which can be defined in the cavity recirculation as:

$$Re_\Omega = \frac{U_c(r - R_c)}{\nu} \quad \text{and} \quad Re_{\Omega,c} = 41.18\sqrt{\frac{R_c}{r - R_c}} \tag{6}$$

with U_c the convection velocity, i.e. the maximum azimuthal velocity inside the cavity, R_c the radius of curvature and r the external radius, i.e. the distance between the recirculation vortex center and the nearest wall. These data are provided from PIV measurements. Figure 19 shows the evolution of Re_Ω versus Re_D for $S/D = 6$. We observe that for any aspect ratio L/D, the vortical instability is observed for Reynolds numbers Re_Ω lower than critical Reynolds number $Re_{\Omega,c}$ except for $L/D = 2$ and $Re_D = 4200$. This is the evidence that cavity centrifugal instability cannot be identified with Taylor-Couette instability.

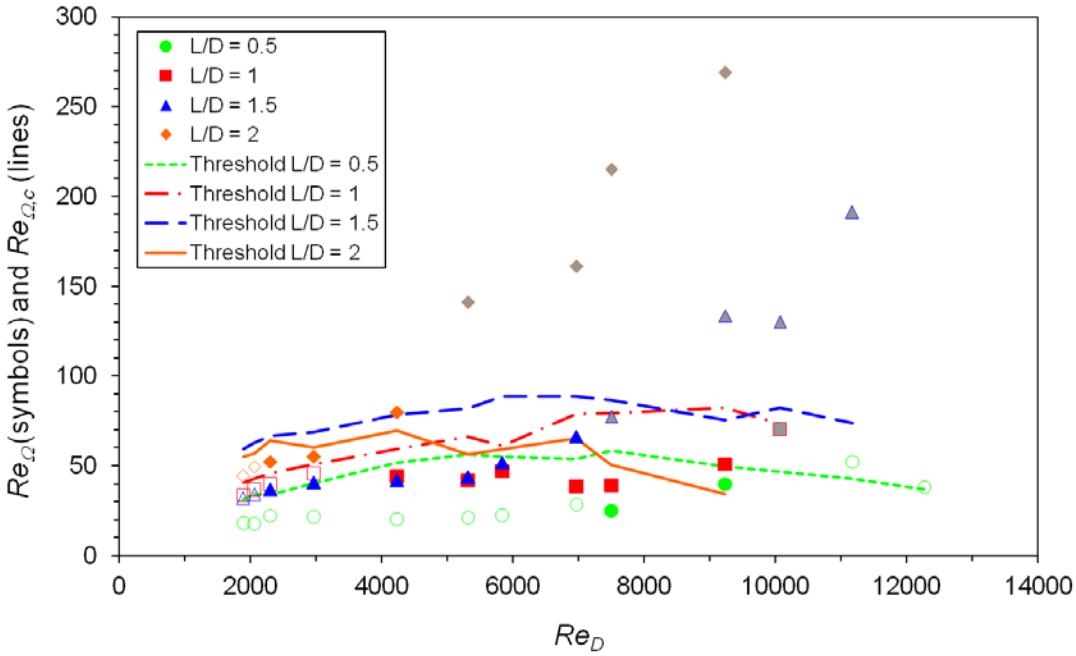

Figure 19: Threshold of the critical Reynolds number for Taylor-Couette instabilities $Re_{\Omega c}$ (lines) versus Re_D (symbols) compared with the measured Reynolds number $Re_{\Omega c}$, for S/D = 6 and four aspect ratios L/D with the following notation conventions: *white-filled symbols* no centrifugal instability, *colored-filled symbols* spanwise instability, *gray-filled symbols* transitional flow.

4.4 Görtler analysis

If we consider the development of vortices induced by the recirculation curvature, we can compare it with the flow on walls with concave curvature leading to Görtler instability. The Görtler number, defined from the curvature radius R_c, the kinematics viscosity of the fluid ν and the velocity inside the cavity U_c developing away from the boundary layer of momentum thickness δ_2 is:

$$G\ddot{o} = \frac{U_c \delta_2}{\nu}\sqrt{\frac{\delta_2}{R_c}} \quad \text{and} \quad k = \frac{2\pi}{\lambda} \tag{7}$$

Values of Görtler number and dimensionless wavenumber are obtained from PIV measurements and are plotted in Figure 20 in comparison with data of previous experiments. The linearized neutral stability curve established by Floryan & Saric (1982) is also plotted on the figure. Hall (1982) concluded that this concept was not meaningful in Görtler boundary layers except in the small wavelength asymptotic limit (Schrader, 2011). Lee & Liu (1992) later revised this view which was resurrected by Bottaro & Luchini (1999), finding it satisfactory above a given value of the local Görtler number. The aim of present study is not to discuss the validity of that theory, but to plot present results for cases where centrifugal instability is developed and compare it with previous experimental results and the existing theory. A global clustering of points with previous experiments is found, above the neutral curve corresponding to the region where the Görtler instability is able to develop.

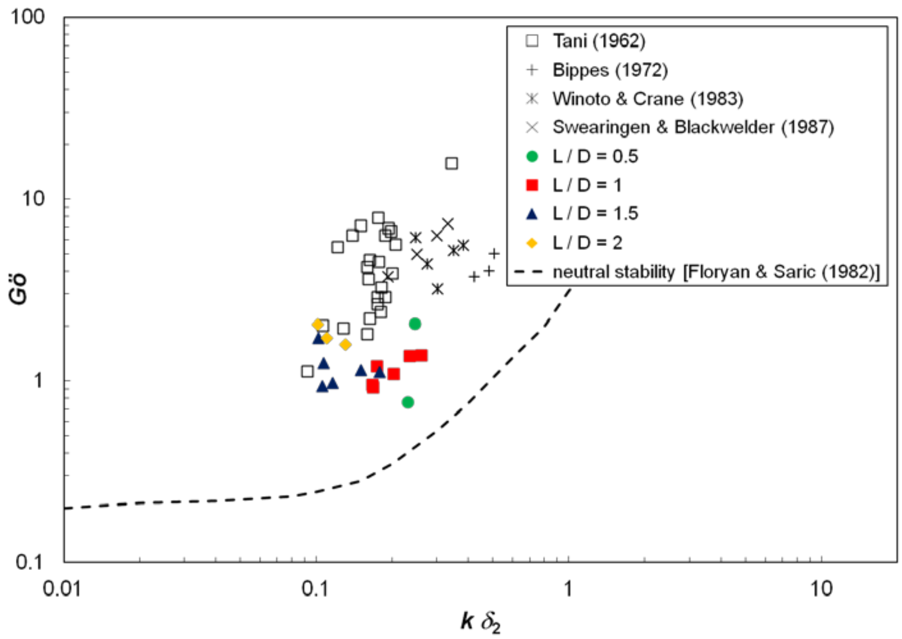

Figure 20: Görtler number versus the dimensionless wavenumber for present measurements and previous ones.

4.5 Stability parameter

As we previously mentioned, the Rayleigh discriminant is sensitive to the recirculation curvature radius and its lateral confinement. Furthermore, the criterion gives information only on regions where the flow is potentially unstable. To get rid of this limitation, a viscous stability parameter for centrifugal instabilities was introduced by Migeon (2000), initially for transient flows, but it can be generalized to time-averaged fields. One can argue that other criteria for centrifugal instability identification exist (Sipp & Jacquin, 2000), but that stability parameter was chosen for a comparison with the aforementioned data of Migeon (2000). For a viscous flow, viscosity tends to stabilize the flow. Therefore there is a competition between destabilizing centrifugal forces and viscous stabilizing forces. Each of these forces tries to diffuse its action. The characteristic time of diffusion depends on the nature of the force but also on the flow conditions, such as the velocity or the cavity geometry. The ratio between the characteristic time of stabilization and the time of destabilization defines the stability parameter. A cylindrical coordinate system is used, with its origin taken in the center of the transverse axis vortex. Eight radial profiles are studied, defining eight azimuths θ, the reference azimuth $\theta = 0$ associated with the straight line passing by the vortex center and the downstream cavity edge (Figure 21). The stability parameter is then defined as:

$$C = \frac{\text{destabilizing centrifugal effects}}{\text{stabilizing viscous effect}} = \frac{\text{stabilizing time}}{\text{destabilizing time}} = \frac{U_c d_i}{\nu}\sqrt{\frac{d_i}{R_c}} \tag{8}$$

U_c is the maximum velocity of the recirculation vortex measured for azimuth θ, R_c the curvature radius for which U_c is measured, ν the fluid kinematic viscosity and d_i is the length of the potentially unsteady region for azimuth θ. The length d_i is a dimension along with the flow is unstable in the sense of Rayleigh discriminant, it is the distance between the maximum of $(r\, U_\theta)^2$ and the intersection of U_θ with the r-axis (Figure 22).

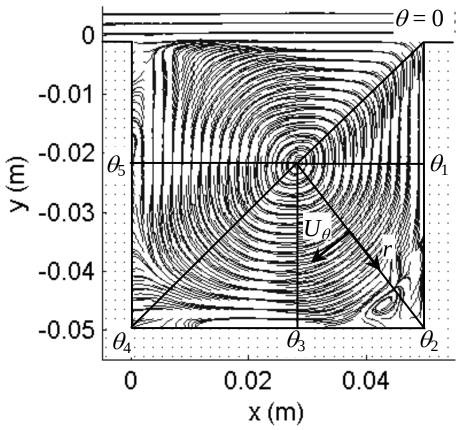

Figure 21: Radial profiles extracted from the average PIV field for $L/D = 1$ and $Re_D = 4230$.

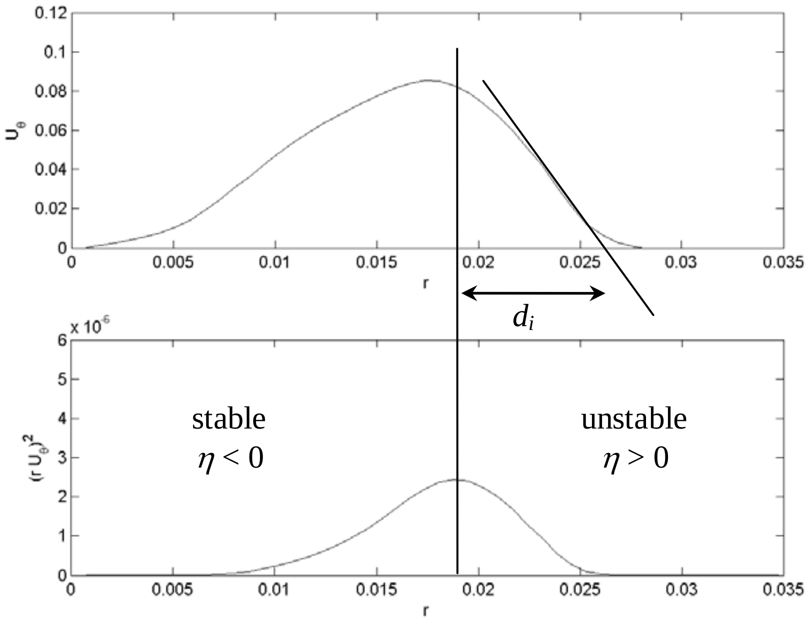

Figure 22: Velocity U_θ and $(rU_\theta)^2$ radial profiles for the azimuth θ_2, $L/D = 1$ and $Re_D = 4230$.

As the flow is not perfectly circular inside the cavity, the stability parameter C is corrected with a shape parameter P_s to take into account the stretching of the recirculation vortex such as for θ_1, $P_s = 1$, for θ_2, $P_s = R_{c,1}/R_{c,2}$, for θ_3, $P_s = R_{c,2}/R_{c,3}$, for θ_4, $P_s = R_{c,3}/R_{c,4}$, and for θ_5, $P_s = R_{c,4}/R_{c,5}$ providing:

$$C = P_s \frac{U_c d_i}{\nu} \sqrt{\frac{d_i}{R_c}} \tag{9}$$

The stability parameter development inside the recirculation cavity flow is shown Figure 23 to Figure 26, for four aspect ratios and different Reynolds numbers. A general increase of C with Re_D is observed. For $L/D = 0.5$ (Figure 23), a maximum is observed around the angle θ_3. It is found for angles between θ_4 and θ_5 for $L/D = 1$, 1.5 and 2, where the potentially unstable region gets a larger extension and the cavity wall confinement is lower in the upstream part of the cavity, relatively to the external flow direction.

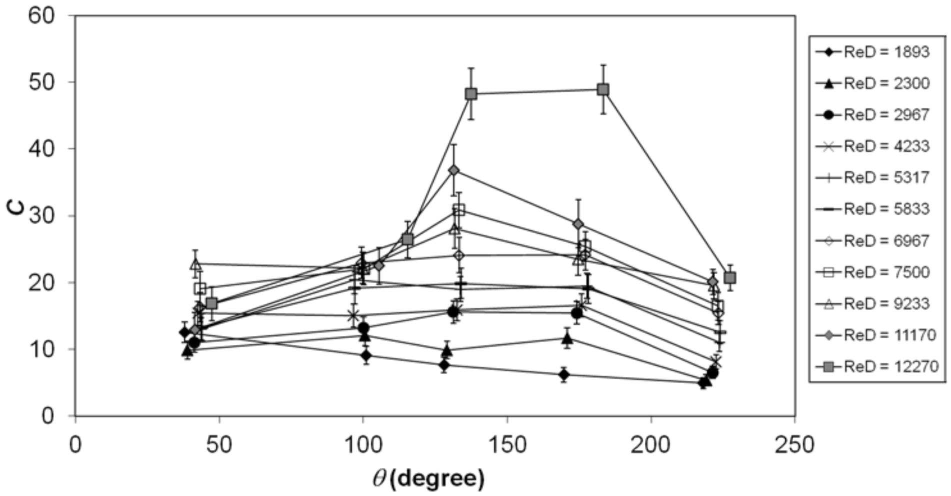

Figure 23: Stability parameter C versus azimuth θ for different Reynolds numbers and L/D = 0.5.

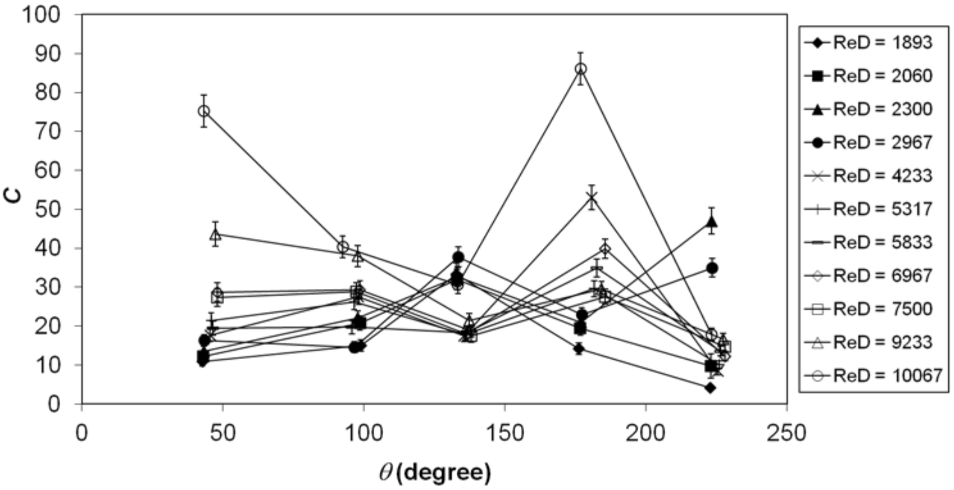

Figure 24: Stability parameter C versus azimuth θ for different Reynolds numbers and L/D = 1.

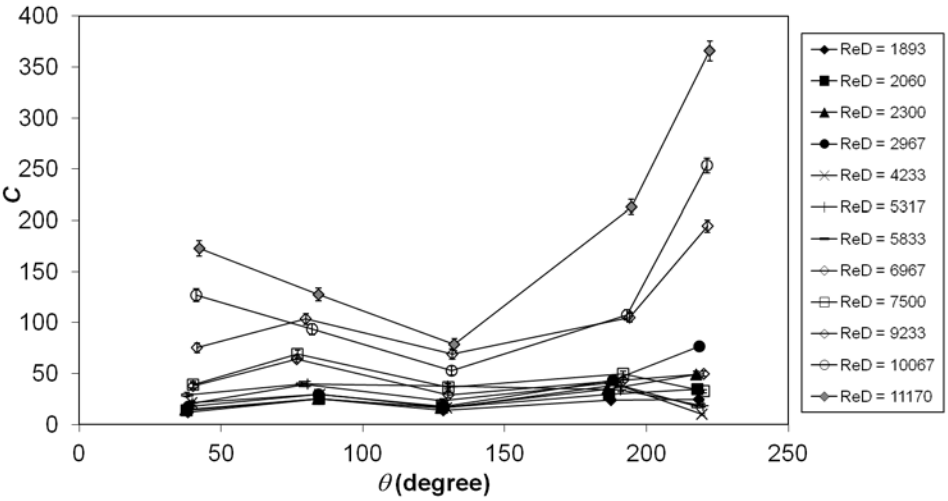

Figure 25: Stability parameter C versus azimuth θ for different Reynolds numbers and L/D = 1.5.

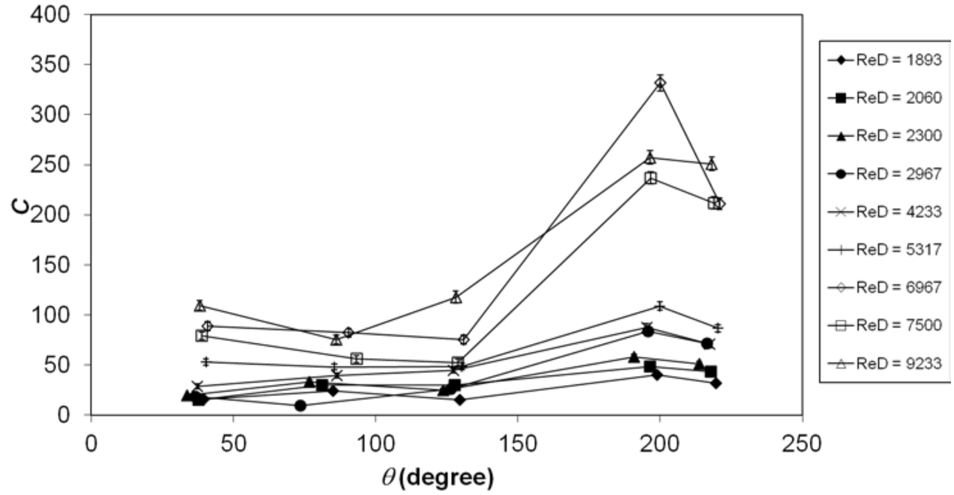

Figure 26: Stability parameter C versus azimuth θ for different Reynolds numbers and L/D = 2.

Comparison of the stability parameter in the present case of shear-layer-driven cavity flow with a lid-driven cavity flow (Migeon, 2000) is presented in Figure 27 for the same order in magnitude of Reynolds numbers and L/D = 1. Larger values of C are observed for the lid-driven cavity in comparison with the shear-layer open flow. C is continuously increasing to the angle θ_5 for the lid-driven cavity while a decrease is observed for the shear-layer-driven cavity, with lower values. Thus the instability level is continuously growing inside the recirculation for the lid-driven flow while it presents two maxima for angles θ_2 and θ_4 for the shear-layer-driven flow and Re_D = 4230. The spatial generation of centrifugal instabilities takes place in different regions between these two cases, although they show a similar quasi-annular shape.

Comparison of the maximum value of C with the identification of centrifugal instabilities, in flow visualizations or Γ_2 fields obtained from PIV measurements, leads to a unique threshold for their generation, varying the Reynolds number and the aspect ratio L/D. In the present study, where the recirculation is induced by a shear-layer, the threshold is 25. If this value is compared to the one found for a recirculation induced by a lid-drive, the threshold found is 80 (Migeon, 2000). As a consequence, it can be said that the shear-layer-driven cavity flow is more unstable than a lid-driven cavity flow. This is confirming the analysis of Sipp & Lebedev (2007), where the instability developing on the shear layer has a strong nonlinear entrainment effect on the inside cavity flow field. This result could explain the difficulty of the observation of vortices resulting from the centrifugal instability in the latter case, where wall surface perturbations have been introduced to force their generation (Migeon, 2000).

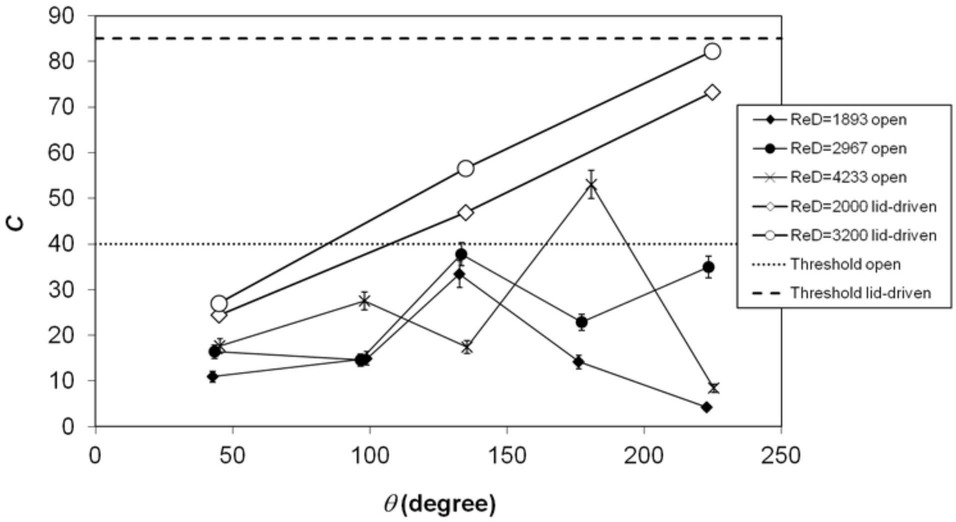

Figure 27: Azimuthal development of the corrected stability parameter for a shear-driven open cavity and a lid-driven cavity (Migeon, 2000) for *L/D* = 1.

5 Conclusion

An open cavity flow driven by the shear-layer development between a boundary layer external flow and a recirculation is investigated with PIV for Reynolds numbers in the range 1900 to 12000 and aspect ratios between 0.5 and 2. The global features show that the cavity flow is characterized by a vortex recirculation and large velocity and turbulence levels are found near the trailing cavity edge where the shear-layer impinges the wall. Development of quasi-annular pairs of counter-rotating vortices is observed for particular parameters, suggesting the rise of a centrifugal instability. These vortices are moving towards the lateral cavity ends; their wavelengths and lateral drift velocity are measured from PIV and compared with data obtained from flow visualizations obtained on the very same experimental set-up. Rayleigh discriminant measured from the time-averaged velocity field shows that the potentially unstable flow region inside the cavity is the external part of the recirculation vortex. Comparisons cases where pairs of counter-rotating vortices are found versus Reynolds number demonstrate that there is a unique threshold of the ratio between the characteristic value of Rayleigh discriminant and the potentially unstable distance. The cavity flow analogy with Taylor-Couette flow theoretical behavior does not seem to provide satisfactory agreement, whereas the confrontation of present experimental data fits with Görtler neutral stability theory. A stability parameter considering the ratio between centrifugal destabilizing effects and stabilizing viscous effects is conducted establishing a unique threshold for a value of that parameter equals to 25 for the present open shear-layer-driven cavity. Available data for a lid-driven cavity exhibit a threshold of 80. Thus, the difference between the two cases proves that the shear-layer-driven cavity flow is controlling the recirculation cavity flow by momentum injection and ejection, providing a lower level of the threshold for the centrifugal instability development. It would be interesting to extend the present study for different values of the span ratio in order to get a global behavior of the cavity flow. In addition, time-resolved PIV would be useful performing the same parametric analysis on time evolving velocity fields to understand the controlling effect of periodic shear-layer injection mechanism. Global stability analyses of cavity flows are available for compressible flow and L/D = 1, 2 and 4 (Brès & Colonius, 2008) or incompressible flow and L/D = 1 (Sipp & Lebedev, 2007, Citro et al. 2014) and L/D between 1.2 and 3 (Meseguer-Garrido et al., 2014). The extension of that approach, for incompressible flow, to other values of L/D is an interesting perspective of this work. Furthermore, the confrontation of the experimental results obtained in this study with the ones obtained with the global stability analysis would be interesting to verify the thresholds established with the present stability parameter.

Acknowledgement

The author gratefully acknowledges Vincent Bourdin, Vincent Gautier and Yves Maire for their technical assistance on the experimental facility and wish to thank François Lusseyran, Luc Pastur and Yann Fraigneau for fruitful discussions during the course of this work.

References

Barbagallo A, Sipp D, Schmid PJ (2009) Closed-loop control of an open cavity flow using reduced-order models, J Fluid Mech 218: 1–50

Barkley D, Gomes GM, Henderson RD (2002) Three-dimensional instabilitiy in flow over a backward-facing step, J Fluid Mech 473:167–190

Basley J, Pastur LR, Lusseyran F, Faure TM, Delprat N (2011) Experimental investigation of global modes in an incompressible cavity flow using time-resolved PIV, Exp Fluids 50: 905–918

Bippes H (1972) Experimentelle Untersuchung des laminar-turbulenten Umschlags an einer parallel angeströmten könkaven Wand, Heidel Akad Wiss Naturwiss Kl 3:103 (also NASA TM–75243, 1978)

Bottaro A, Luchini P (1999) Görtler vortices: are they amenable to local eigenvalue analysis? Eur. J. Mech. B/Fluids 18:47–65

Braun MJ, Choi FK, Zhou M (1993) The effects of a hydrostatic pocket aspect ratio, and its supply orifice position and attack angle on steady-state flow pattern, pressure and shear characteristics, J Tribol 115:678–685

Brès GA, Colonius T (2008) Three-dimensional instabilities in compressible flow over open cavities, J Fluid Mech 599:309–339

Buckholz RH (1986) The functional role of wing corrugation in living systems, J Fluids Eng 108:93–97

Chabni A (1997) Étude par méthodologie de type Simulation des Grosses Structures de la dynamique de l'interaction et des échanges entre une couche limite et une encoche, PhD thesis, Université Paris XI (in french)

Charwat AF, Roos JN, Dewey FC, Hitz JA (1961) An investigation of separated flows. Part 1: the pressure field, J Aero Sci 28:457-470

Chatellier L, Laumonier Y, Gervais Y (2004) Theoretical and experimental investigation of low Mach number turbulent cavity flows, Exp Fluids 36:728–740

Chicheportiche J, Merle X, Gloerfelt X, Robinet JC (2008) Direct numerical simulation and global stability analysis of three-dimensional instabilities in a lid-driven cavity, Comptes Rendus Mécanique 336(7): 586–591

Citro V, Giannetti F, Brandt L, Luchini P (2014) Global and asymptotic stability analysis of open cavity flows, J Fluid Mech (under review)

Crow SC (1970) Stability theory for a pair of trailing vortices, AIAA J 8: 2172–2179

Douay CL (2014) Étude expérimentale paramétrique des propriétés et transitions de l'écoulement intra-cavitaire en cavité ouverte et contrôle de l'écoulement, Ph. D. thesis, Université Pierre-et-Marie-Curie, Paris (in french)

Douay CL, Faure TM, Lusseyran F (2013) Stereoscopic PIV using optical flow: application to a cavity recirculation, Exp Fluids 54: 1579, 15 p.
Drazin PG Reid WH (1981) Hydrodynamic stability, Cambridge University Press
Fang LC, Nicolaou D, Cleaver JW (1999) Transient removal of a contaminated fluid from a cavity, Intl J Heat Fluid Flow 20:605–613
Faure T (2008) Dynamique des fluides appliquée, Applications à l'aérodynamique, Dunod (in french)
Faure TM, Adrianos P, Lusseyran F, Pastur LR (2007) Visualizations of the flow inside an open cavity at medium range Reynolds numbers, Exp Fluids 42:169–184
Faure TM, Lusseyran F, Gougat P, Launay F. (2006) Experimental investigation of the flow distribution inside a tubular heat exchanger, J Fluids Engng 128:1218–1227
Faure TM, Pastur LR, Lusseyran F, Fraigneau Y, Bisch D (2009) Three-dimensional centrifugal instabilities development inside a parallelepipedic open cavity of variable shape, Exp Fluids 47:395–410
Floryan JM, Saric WC (1982) Stability of Görtler vortices in boundary layers, AIAA J 20:316–324
Forestier N, Jacquin L, Geffroy P (2003) The mixing layer over a deep cavity at high-subsonic speed, J Fluid Mech 475:101–145
Gloerfelt X (2009) Cavity noise, Von Kármán Institute Lecture Series 169 p.
Gomez F, Gomez R, Theofilis V (2014) On three-dimensional global linear instability analysis of flows with standard aerodynamics codes. Aerosp. Sci. Technol. 32:223–234
Graftieaux L, Michard M Grosjean N (2001) Combining PIV, POD and vortex identification algorithms for the study of unsteady turbulent swirling flows, Meas Sci Techno 12:1422–1429
Guermond JL, Migeon C, Pineau G, Quartapelle L (2002) Start-up flows in a three-dimensional rectangular driven cavity of aspect ratio 1:1:2 at Re = 1000, J Fluid Mech 45:169–199
Haigermoser C, Scarano F, Onorato M (2009) Investigation of the flow in a circular cavity using stereo and tomographic particle image velocimetry, Exp Fluids 46:517–526
Hall P (1982) Taylor–Görtler vortices in fully developed or boundary-layer flows: linear theory, J Fluid Mech 124:475–494
Hunt JCR, Wray AA, Moin P (1988) Eddies, stream and convergence zones in turbulent flows, Center for Turbulence Research Report CTR-S88: 193
Jeong J, Hussain F (1995) On the identification of a vortex, J Fluid Mech 285:69–94
Kegerise MA, Spina EF, Garg GS, Cattafesta III LN (2004) Mode-switching and nonlinear effects in compressible flow over a cavity, Phys Fluids 16:678–687
Kuo CH, Huang SH (2001) Influence of flow path modification on oscillation of cavity shear layer, Exp Fluids 31:162–178
Larchevêque L, Sagaut P, Lê TH, Comte P (2004) Large-eddy simulation of a compressible flow in a three-dimensional open cavity at high Reynolds number, J Fluid Mech 516:265–301
Lee K, Liu, JTC (1992) On the growth of mushroom-like structures in nonlinear spatially developing Görtler vortex flow, Phys Fluids A 4:95–103
Lin JC, Rockwell D (2001) Organized oscillations of initially turbulent flow past a cavity, AIAA J 39:1139–1151
Liou T, Liao C (1997) Study of pulsative flows in lateral aneurysm models on a straight parent vessel using particle tracking velocimetry, The first Pacific Symposium on Flow Visualization and Image Processing, Honolulu, 639–644
Luchini P, Bottaro A (2014) Adjoint equations in stability analysis, Annu Rev Fluid Mech 46(1):493–517
Merle X, Alizard F, Robinet JC (2010) Finite difference methods for viscous incompressible global stability analysis, Computers & Fluids 39: 911–925

Meseguer-Garrido F, de Vicente J, Valero E, Theofilis V (2011) Effect of aspect ratio on the three-dimensional global instability analysis of incompressible open cavity flows, 6th AIAA Theoretical Fluid Mechanics Conference, 27-30 June 2011, Honolulu, Hawaii, AIAA paper 2011-3605
Meseguer-Garrido F, de Vicente J, Valero E, Theofilis V (2014) On linear instability mechanisms in incompressible open cavity flow, J. Fluid Mech 752:219–236
Michard M, Favelier T (2004) Développement d'un critère d'identification de structures tourbillonnaires adapté aux mesures de vitesse par PIV, 9ème Congrès Francophone de Vélocimétrie Laser, Brussels (Belgium), September 14-17 (in french)
Migeon C (2000) Contribution à l'analyse de l'écoulement tridimensionnel instable s'établissant à l'intérieur de cavités cylindriques, PhD thesis, Université de Poitiers (in french)
Migeon C (2002) Details on the start-up development of the Taylor-Görtler-like vortices inside a square-section lid-driven cavity for 1,000 ≤ Re ≤ 3,200, Exp Fluids 33:594–602
Migeon C, Pineau G, Texier A. (2003) Three-dimensionality development inside standard parallelepipedic lid-driven cavities at Re = 1000, J Fluids Structs 17:717–738
Mutabazi I, Hegseth JJ, Andereck DA, Weisfreid JE (1990) Spatiotemporal pattern modulations in the Taylor-Dean system, Phys. Rev. Lett. 64(15): 1729–1733
Neary MD, Stephanoff KD (1987) Shear-layer-driven transition in rectangular cavity, Phys Fluids 30:2936–2946
Quénot GM (1992) The orthogonal algorithm for optical flow detection using dynamic programming, Proc IEEE ICASSP 3:249–252
Rayleigh JS (1916) On the dynamics of evolving fluids, Scientific papers 6:447–453
Reulet P, Esteve MJ, Millan P, Riethmuller ML (2002) Experimental characterization of the flow within a transitional rectangular cavity, Journal of Flow Visualization and Image Processing 9:2-3
Rossiter JE (1964) Wind tunnel experiments on the flow over rectangular cavities at subsonic and transonic speeds, RAE Technical Report 64037
Rowley CW, Colonius T, Basu, AJ (2002), On self-sustained oscillations in two-dimensional compressible flow over rectangular cavities, J Fluid Mech 455:315-346
Sarohia V (1977) Experimental investigation of oscillations in flows over shallow cavities, AIAA J 15:984–991
Savelsberg R, Castro I (2008) Vortex flows in open cylindrical-section cavities, Exp Fluids 46:485–497
Schlichting H (1960) Boundary layer theory, McGraw-Hill
Schmid PJ (2007) Nonmodal stability theory, Annu. Rev. Fluid Mech., 39:129–162
Schrader LU, Brandt L, Zaki TA (2011) Receptivity, instability and breakdown of Görtler flow, J Fluid Mech 682:362–396
Siegmann-Hegerfeld T, Albensoeder S, Kuhlmann HC (2013) Three-dimensional flow in a lid-driven cavity with width-to-height ratio of 1.6, Exp Fluids 54:1526–1534
Sipp D (2012) Open-loop control of cavity oscillations with harmonic forcings, J Fluid Mech 708:439–468
Sipp D, Jacquin L (2000) Three-dimensional centrifugal-type instabilities of twodimensional flows in rotating systems, Phys Fluids 12:1740–1748
Sipp D, Lebedev A (2007) Global stability of base and mean flows: a general approach and its applications to cylinder and open cavity flows, J Fluid Mech 593:333–358
Sipp D, Marquet O, Meliga P, Barbagallo A (2010) Dynamics and control of global instabilities in open-flows: a linearized approach, Appl Mech Rev 63:030801, 26 p.
Swearingen JD, Blackwelder RF (1987) The growth and breakdown of streamwise vortices in the presence of a wall, J Fluid Mech 182:255–290

Tani I (1962) Production of longitudinal vortices in the boundary layer along a concave wall, J Geophys Res 67:3075–3080
Tritton D J (1988) Physical fluid dynamics, Second Edition, Oxford Science Publications
de Vicente J, Basley J, Meseguer-Garrido F, Soria J, Theofilis V (2014) Three-dimensional instabilities over a rectangular open cavity: from linear stability analysis to experimentation, J. Fluid Mech 748:189–220
Winoto SH, Crane RI (1980) Vortex structure in laminar boundary layers on a concave wall, Intl J Heat Fluid Flow 2:221–231
Yamouni S, Sipp D, Jacquin L (2013) Interaction between feedback aeroacoustic and acoustic resonance mechanisms in a cavity flow: a global stability analysis. J. Fluid Mech 717:134–165.